1985ApJ...298...34S

THE ASTROPHYSICAL JOURNAL, 298:34–57, 1985 November 1
© 1985. The American Astronomical Society. All rights reserved. Printed in U.S.A.

RELATIVISTIC STELLAR DYNAMICS ON THE COMPUTER. I. MOTIVATION AND NUMERICAL METHOD

STUART L. SHAPIRO AND SAUL A. TEUKOLSKY
Center for Radiophysics and Space Research, and Departments of Astronomy and Physics, Cornell University, Ithaca, New York
Received 1985 February 4; accepted 1985 April 24

ABSTRACT

This is the first of a series of papers on the numerical solution of Einstein's equations for the dynamical evolution of a *collisionless* gas of particles in general relativity. The initial analysis is restricted to spherically symmetric systems, but the gravitational field can be arbitrarily strong and particle velocities can approach the speed of light. The computational method uses the tools of numerical relativity and N-body particle simulation to follow the full nonlinear behavior of these systems. Specifically, we solve the Vlasov equation in general relativity by particle simulation. The gravitational field is integrated using the $3 + 1$ formalism of Arnowitt, Deser, and Misner.

Physical applications include the stability of relativistic star clusters, the binding energy criterion for stability, the collapse of star clusters to black holes, relativistic violent relaxation, and the stability of Newtonian polytropic star clusters. Astrophysical issues addressed include the possible origin of quasars and active galactic nuclei via the collapse of dense star clusters to supermassive black holes, and possible sites for dark matter following the collapse of collisionless bound matter in the early universe.

In this paper we derive the fundamental equations for the problem, describe our numerical method for solving them, and report on a series of test-bed calculations used to check the equations and our algorithm. We find that the method is extremely accurate, even in the case of black hole formation.

Subject headings: black holes — numerical methods — relativity — stars: stellar dynamics

I. INTRODUCTION

Gravitation physics, like many other branches of nonlinear physics, has made significant advances with the advent of computers. Two areas of gravity research in particular have been the subject of intensive computational efforts in recent years. One area, loosely called "N-body physics," is a variation of the classical N-body problem. Stripped to its bare essentials, this problem requires that a large number N of self-gravitating, but otherwise noninteracting, point particle masses be evolved numerically in time, starting from some given set of initial particle positions and velocities. The governing dynamical equation is Newton's law of motion in a many-body, Newtonian (Coulomb) gravitational field. The other area of intensive research is "numerical relativity," a considerably younger pursuit. It concentrates on integrating forward in time on the computer the coupled Einstein equations of general relativity for the gravitational metric field and matter distribution, again starting from some well-posed initial data. To date, the matter distributions of interest have all been those of a fluid gas (and, typically, a perfect fluid) and are therefore controlled by the equations of relativistic hydrodynamics.

This paper is the foundation of a series of three (cf. Shapiro and Teukolsky 1985*a*, *b*) which attempt, essentially for the first time, to link the two, heretofore distinct, computational endeavors described above. Specifically, we present in these papers (hereafter Papers I, II, and III) numerical solutions of the Einstein equations for the dynamical evolution of a *collisionless* gas in general relativity. For our initial investigation, we restrict the analysis to spherically symmetric systems. Our focus is on dynamical scenarios involving strong gravitational fields and high particle velocities approaching the speed of light. We thereby extend previous work on the N-body problem to the fully relativistic domain. We also extend previous work in numerical relativity to the regime of collisionless matter.

The analysis we present may casually be referred to as "relativistic stellar dynamics on the computer." Indeed, many of the key applications of our calculations address outstanding issues concerning the dynamical behavior of relativistic star clusters. However, our results have far wider applicability, in that the matter fields need not be identified with stars per se but with *any* gas of collisionless, self-gravitating particles. It is more appropriate, then, to regard our computations very generally as numerical solutions of the collisionless Boltzmann (or Vlasov) equation for spherical systems in general relativity.

The motivation for tackling this problem is at least threefold: computational, theoretical, and astrophysical. Computationally, "field theory on a space-time lattice" has become a booming enterprise in recent years. The activity is pursued by theorists in many diverse branches of physics, including solid-state, particle, and plasma physics, astrophysics, hydrodynamics, and relativity. Solving the relativistic Vlasov equation falls into this broad category of computational problems, the field being the gravitational metric of general relativity. Even for spherical systems, the basic problem results in a highly nonlinear, many-body, multidimensional (in phase space), and time-dependent coupled set of differential equations. These "attributes" are all particularly appealing to a computational physicist. Progress achieved in solving such a nonlinear physics problem often transcends the narrow field in which the problem was originally posed and the specific applications initially under investigation. This notion in particular underlies much of our rationale for tackling the collisionless gas problem in general relativity.

© American Astronomical Society • Provided by the NASA Astrophysics Data System

1985ApJ...298...34S

Theoretically, the problem addresses several major, unresolved issues in relativistic stellar dynamics. Thus, for example, there exist as yet only sufficient, but not necessary, criteria for the radial stability of a spherical relativistic star cluster (Ipser 1980). Moreover, the nonlinear evolution and final fate of an unstable cluster have never been demonstrated, although one can conjecture (cf. Zel'dovich and Podurets 1965; Fackerell, Ipser, and Thorne 1969) that it is likely to be catastrophic collapse to a black hole. Previous work, based on perturbation theory (see § II), has been unable to resolve the first issue satisfactorily and unable to address the second issue at all. Fully nonlinear, time-dependent calculations, like the ones presented below, are required to settle these important questions.

Astrophysically, our study of the dynamical evolution of collisionless systems in general relativity has many potential applications in stellar dynamics, cosmology, and gravitational wave astronomy and some important associated observational consequences. This statement may seem surprising when one recalls that in the late 1960s and early 1970s, relativistic stellar dynamics was pursued in large measure to find gravitationally bound, high-redshift, stable systems to explain the high redshifts observed in quasars. Obviously, this particular pursuit is no longer very relevant today. However, explaining quasars and active galactic nuclei (AGNs) is still a burning issue. Lately it has become increasingly evident that quasars, AGNs, and other intense extragalactic radio sources are powered by jets of gas and magnetic fields and that each jet is produced by a compact supermassive object ($M \gtrsim 10^7\ M_\odot$) in the nucleus of a galaxy (cf. Begelman, Blandford, and Rees 1984). A supermassive black hole is the likely candidate for the compact object. But the puzzle remains—how and under what circumstances did these supermassive black holes form?

Once again, relativistic stellar dynamics may provide the essential clue to this puzzle. Previewing our discussion in Paper III, it is well known that the secular (Fokker-Planck) evolution of a large, self-gravitating N-body system is inevitably to states of ever increasing central redshift (a process referred to as "core collapse" or the "gravothermal catastrophe"; cf. Spitzer 1975, 1985; Lightman and Shapiro 1978). Could catastrophic collapse to a supermassive black hole be the endpoint evolutionary state of a dense, though initially Newtonian, stellar system? Are there plausible circumstances for which realistic galactic nuclei are likely to evolve according to this scenario? Is there any observational support for this idea? We provide answers to these intriguing and potentially important questions in Paper III but postpone addressing them now until we lay firm theoretical groundwork and provide concrete computational "data" in Papers I and II. It should nevertheless be clear already that the numerical problem we have posed is potentially interesting and important astrophysically.

From all three viewpoints— computational, theoretical, and astrophysical—the computations we summarize below nicely complement previous studies in numerical relativity (see, e.g., Smarr 1979; Deruelle and Piran 1983, and references therein). All these have focused on the behavior of ideal *fluid* systems in general relativity and have employed a perfect gas stress-energy tensor for the matter fields appearing in Einstein's equations. Our present focus on self-gravitating *collisionless* particles has two advantages over this approach: (1) it allows us to address entirely new classes of astrophysical objects characterized by strong gravitational fields and high particle velocities, such as relativistic star clusters and clusters of massive neutrinos, axions, photinos, etc., all of which are collisionless systems; and (2) it allows us to integrate Einstein's equations on the computer without additional complications induced by relativistic hydrodynamics. Here we refer in particular to numerical complications inevitably arising from shocks and other discontinuities. Thus, the replacement of the matter energy-momentum conservation equations for fluids ($\nabla \cdot \boldsymbol{T} = 0$, where $\boldsymbol{T}$ is the fluid stress-energy tensor) by the corresponding geodesic equations for noninteracting particles may provide somewhat cleaner and more accurate insight into the nature of the Einstein field equations for a strong-field metric without the excess baggage and numerical difficulties encountered in fully relativistic hydrodynamics.

On the other hand, evolving a relativistic collisionless particle distribution is no less challenging a computational problem than evolving a relativistic fluid gas. Indeed, as Zel'dovich and Podurets (1965) recognized twenty years ago, "the problem is more difficult than the nonstationary hydrodynamical problem, since in the problem concerning particles the state of matter at each point is determined not by several quantities (density, pressure, temperature, velocity), but by a function of the momentum vector." Of course, both studies—the evolution of relativistic fluid and of collisionless gases—are absolutely essential. We simply seek to fill a vaccum in the computational literature by addressing the collisionless problem here.

Our plan of presentation is as follows: Paper I provides introductory discussion and background to the problem, outlines our basic computational method, and summarizes the performance of our code when used to solve a large number of carefully constructed test-bed calculations. Specifically, § II presents a brief history of previous work in relativisitic stellar dynamics. Section III provides the fundamental equations for the matter and metric field quantities. Section IV summarizes the overall strategy we employ to solve the equations numerically. Section V discusses the procedure by which we prepare initial data for our computations. Section VI summarizes the nature of the test-bed calculations designed to check our numerical algorithms and overall method. Section VII provides specific numerical results for some of the more interesting and stringent of these test calculations.

In Paper II, we apply our code to address several outstanding theoretical issues in relativistic stellar dynamics. In Paper III we discuss the possibility that quasars and AGNs may arise from the collapse of dense stellar systems (i.e., evolved galactic nuclei) to supermassive black holes. Readers interested only in the theoretical results and possible astrophysical implications of our computations and not in details of our method may skip Paper I (following § II) and proceed directly to Papers II and III.

II. HISTORICAL PERSPECTIVE

As a guide to solving the spherically symmetric, collisionless gas problem in general relativity on the computer, it is useful to recall the salient features and limitations of earlier (mostly analytic) work on the subject.

The field of relativistic stellar dynamics was effectively launched by Einstein (1939), who constructed static, spherically symmetric, collisionless clusters of gravitating particles to investigate the physical significance of the Schwarzschild singularity. Einstein assumed that the particles all moved in circular orbits. He showed that $2GM/RC^2$, where M is the total mass-energy and R is the areal radius of a cluster, could never

© American Astronomical Society • Provided by the NASA Astrophysics Data System

1985ApJ...298...34S

reach unity for such a system, so that the Schwarzschild singularity could never be realized.[1]

Some years earlier, actually, Synge (1934) and Walker (1936) had laid the formal groundwork for more general discussions of collisionless distributions in relativity, while Walker derived the collisionless Boltzmann equation satisfied by the distribution function (see Fackerell 1968 for a slightly expanded summary of this early work).

For the most part, however, a casual perusal of the literature suggests that the field of relativisitic stellar *dynamics* could have been named more aptly the study of relativistic stellar *statics*. That is, beginning with the spherical, circular orbit models of Einstein (1939) (see also Zapolsky 1968), and extending through the more realistic, spherical, isotropic models of Zel'dovich and Podurets (1965); Fackerell (1968, 1970); Fackerell, Ipser, and Thorne (1969); Ipser and Thorne (1968); Ipser (1969*a*, *b*, 1980); Katz and Horwitz (1974); and Suffern and Fackerell (1976), previous work has focused on the construction of static solutions of collisionless systems in general relativity and the establishment of criteria for their stability (see Zel'dovich and Novikov 1971; Misner, Thorne, and Wheeler 1973 for many more details and references). As noted in § I, much of this work was originally motivated by the discovery of quasars and the subsequent attempt to find *intrinsically* high redshift, stable, equilibrium systems to explain them. A number of interesting questions were raised in these studies. Can stable models with arbitrarily large redshifts be constructed? What are the perturbation equations for the radial deformation of spherical, equilibrium systems? Do there exist global stability criteria for the onset of gravitational collapse along equilibrium sequences of collisionless configurations, as is the case for fluid stars in general relativity? And so on.

A number of these intriguing questions were answered by these original investigations, which for the most part applied linear perturbation techniques to numerical models of spherical, equilibrium configurations. For example, following the suggestions by Zel'dovich and Podurets (1965) that sufficiently compact, high-redshift objects would be unstable to gravitational collapse, Ipser and Thorne (1968) formulated the theory of the stability of collisionless, spherical configurations against radial perturbations in the form of a variational principle. Ipser (1969*b*) then successfully reduced this variational principle to a form suitable for analyzing, by use of trial functions, the radial stability of both isothermal and polytropic configurations, provided their equilibrium density distributions were not too centrally condensed. Fackerell (1970) extended this approach to study very centrally condensed clusters ("extreme core-halo configurations"). The upshot of this work was the numerical discovery that along a sequence of equilibrium configurations parameterized by z_c, the central redshift of the system, the onset of instability occurred very near the point of maximum fractional binding energy, $z_c \gtrsim 0.5$, independent of the nature of the models. The result was subsequently rigorized by Ipser (1980), who proved that appropriate one-parameter sequences of spherical, equilibrium configurations were stable at least up to the first maximum of the fractional binding energy.

Although appreciable progress was thus achieved in resolving some of the important issues, many of the key questions remained unsolved. For example, the inability to prove both a sufficient *and* necessary binding energy criterion for radial stability restricted the applicability of the binding energy curve as a stability diagnostic for collisionless systems. This contrasts with the situation for spherical fluid configurations (stars) in general relativity, for which the binding energy maximum rigorously locates the onset of radial instability.[2] More significantly, the nonlinear evolution and ultimate fate of an unstable collisionless cluster could only be conjectured in these earlier studies.

Perhaps the most interesting and important concept to emerge from this previous work was the speculation, originally due to Zel'dovich and Podurets (1965), that unstable clusters inevitably undergo catastrophic collapse to a black hole (see also Fackerell, Ipser, and Thorne 1969, Zel'dovich and Novikov 1971, and Misner, Thorne, and Wheeler 1973, who all subsequently endorsed this conjecture). Their qualitative scenario was recounted by Zel'dovich and Novikov (1971), who wrote, "The physical picture of the collapse in this case is an increase of the core mass, accompanied by a transformation of formerly stable orbits into inward spirals, which lead the core and accompanying stars into their collective gravitational radius .... A numerical investigation of such collapse is badly needed, but no one up to now has had the fortitude to attempt it."

Part of the purpose of our series of papers is to reexamine many of the unresolved issues in relativistic stellar dynamics mentioned above. In particular, we muster the necessary computational fortitude to solve the problem of catastrophic collapse of an unstable equilibrium cluster to a black hole. To do so requires application of the mathematical tools and associated computational techniques which have come to be associated with "numerical relativity." This young discipline postdates, for the most part, the early work in relativistic dynamics which we have sketched above. Numerical relativity consists of solving on the computer the initial value (Cauchy) problem in general relativity. The typical starting point in this endeavor is the ADM approach to general relativity (Arnowitt, Deser and Misner 1962). ADM cast the Einstein equation into a form suitable for evolving spacetimes into the future from well-posed initial data specified on a spacelike hypersurface. In this formulation of general relativity, four-dimensional spacetime is split into 3 + 1 dimensional space + time. This decomposition yields (1) "constraint" or "initial value" equations, which contain no time derivatives and relate field quantities (i.e., metric coefficients) on spacelike hypersurfaces; and (2) "evolution" equations, which contain all the time derivatives and enable one to evolve field quantities from one time slice (i.e., spacelike hypersurface) to the next. (For extensive discussion of the geometric significance of the ADM equations and some examples of their numerical implementation, see articles in Smarr 1979 and Deruelle and Piran 1983, and references therein.)

We have ourselves employed the ADM equations previously

[1] Einstein (1939) went on to infer that "'Schwarzschild singularities' do not exist in physical reality .... The 'Schwarzschild singularity' does not appear for the reason that matter cannot be concentrated arbitrarily." Although true for static, nonsingular, equilibrium configurations, Einstein's statement is of course not true for dynamic spacetimes, which can give rise to black holes and spacetime singularities. See § VII for numerical demonstrations.

[2] Suffern and Fackerell (1976) concluded that in the case of a collisionless sequence "The confirmation or otherwise of this conjecture must await the development of more powerful methods for studying the dynamic stability of relativistic star clusters."

© American Astronomical Society • Provided by the NASA Astrophysics Data System

1985ApJ...298...34S

to successfully follow on the computer the spherical, adiabatic collapse of a *fluid* star to a Schwarzschild black hole (Shapiro and Teukolsky 1979, 1980). Our integrations were able to track the formation and growth of the black hole far into the future (i.e., for many crossing timescales $\Delta t \gg M$ after the appearance of a trapped surface) without encountering physical or numerical singularities. These integrations generated the first numerically reliable spacetimes for the collapse of a fluid with internal pressure to a black hole. We have drawn heavily on this experience in constructing our new code, reported below, which follows the dynamical evolution, including catastrophic collapse to a black hole, of a collisionless, spherical gas in general relativity.

III. BASIC EQUATIONS

The metric is written in isotropic form,

$$ds^2 = -(\alpha^2 - A^2\beta^2)dt^2 + 2A^2\beta dr dt + A^2(dr^2 + r^2 d\theta^2 + r^2 \sin^2\theta d\phi^2) . \quad (1)$$

Here α and β are the lapse and shift functions of ADM; see also Smarr and York (1978*a*, *b*). We use units with $c = G = 1$.

a) Matter Equations

We are considering the matter to be a smooth gas of *collisionless* particles, so the stress-energy tensor is simply the sum of the stress-energy tensors for the individual particles. This would be an infinite sum of δ-functions, but it can be written equivalently by grouping together those particles at a point in spacetime that have the same mass and 4-velocity. Then the stress-energy tensor is

$$T^{\mu\nu} = \sum_A m_A n_A u_A{}^\mu u_A{}^\nu \quad (2)$$

Here m_A is the rest mass of category A particles, $u_A{}^\mu$ is their 4-velocity, and n_A is the number density measured in the comoving frame of the category A particles. The quantity n_A is proportional to a δ-function in the limit of point particles, but it can be treated it as a continuous, averaged quantity when the number of particles is infinite and the particle distribution is smooth.

The equation of motion of the particles is simply the geodesic equation,

$$u^\mu{}_{;\nu} u^\nu = 0 , \quad (3)$$

where a semicolon denotes covariant differentiation. We drop the label A when referring to any one of the particles. This equation follows from the conservation of stress-energy,

$$T^{\mu\nu}{}_{;\nu} = 0 , \quad (4)$$

and the conservation of particles,

$$(nu^\nu)_{;\nu} = 0 . \quad (5)$$

We will solve the N-body problem by the field-particle method used widely in nonrelativistic stellar dynamics and in plasma physics: given the positions and velocities of the particles at any instant, we bin them into a smooth density function. We then use this smooth density to compute the gravitational field. Finally, we move the particles in the mean field to get new positions and velocities.

Throughout this paper we assume *spherical symmetry*. This means that each particle is moving in a central potential, with its motion confined to a plane. The orbital planes are taken to be uniformly distributed in a sphere, with equal numbers of corotating and counterrotating orbits. Thus each group of particles whose orbits differ only in the orientation of these planes is effectively replaced by a spherical shell. The radial motion of the shell is the same as the radial motion of any one of its constituent particles. In particular, we may consider an orbit in the equational plane, so that

$$u_\theta = 0 . \quad (6)$$

Conservation of angular momentum follows from ϕ being an ignorable coordinate:

$$u_\phi = \text{constant} . \quad (7)$$

The geodesic equation (3), together with the metric (1), gives, after some calculation,

$$\frac{dr}{dt} = \frac{u_r}{A^2 u^0} - \beta \quad (8)$$

$$\frac{du_r}{dt} = -u^0 \alpha \alpha_{,r} + u_r \beta_{,r} + \frac{u_r{}^2}{u^0}\frac{A_{,r}}{A^3} + \frac{u_\phi{}^2}{u^0}\left(\frac{1}{r^3 A^2} + \frac{A_{,r}}{r^2 A^3}\right) . \quad (9)$$

Here a comma denotes a partial derivative.

In the Newtonian limit, $A \to 1$, $u^0 \to 1$, $\beta \to 0$, $\alpha \to 1$, and $\alpha_{,r} \to \Phi_{,r}$, where Φ is the Newtonian potential. We thus recover the usual equations for a central potential.

The normalization of the 4-velocity,

$$u_\mu u^\mu = -1 , \quad (10)$$

gives

$$\alpha u^0 = \left(1 + \frac{u_r{}^2}{A^2} + \frac{u_\phi{}^2}{A^2 r^2}\right)^{1/2} . \quad (11)$$

Thus, given the metric at any time t, equations (8), (9), and (11) are used to solve for the new positions and 4-velocities of the particles. (Our decision to use u_r rather than u^r as a fundamental quantity is based on the resulting simplification of the equations.)

b) Metric Equations

The simplest conceptual way to solve Einstein's equations numerically is to choose a time slice $t = 0$, say. Given suitable initial data (values of certain metric field variables) at $t = 0$, Einstein's equations allow one to propagate the initial data forward in time. In this approach, Einstein's equations are *second-order* differential equations in t.

Experience suggests that a better approach is to regard time derivatives of the metric as "velocities" or "momenta." One can then write Einstein's equations as *first-order* differential equations in t for the "coordinates" and "momenta." This "3 + 1" Hamiltonian approach was introduced in the form adopted by most numerical relativists by ADM, although for different purposes.

A subtlety in numerical relativity is how to choose the coordinates. In general relativity, any smooth labeling of events in spacetime by coordinates is permissible. For example, consider a slicing of spacetime by time slices $t = 0$, $t = dt$, $t = 2dt$, ..., and consider an observer at rest on the slice $t = 0$. Such an observer's worldline is normal to the slice. After the coordinate time dt has elapsed, let the amount of proper time that has elapsed for the observer be $d\tau$. Since the slicing, or choice of t-coordinate, was arbitrary, there is an arbitrary proportion-

© American Astronomical Society • Provided by the NASA Astrophysics Data System

1985ApJ...298...34S

ality between dt and $d\tau$:

$$d\tau = \alpha dt \, . \tag{12}$$

This defines the *lapse function* α.

There is still further freedom in the choice of coordinates. Consider a second observer who moves from the point labeled by spatial coordinates x^i at $t = 0$ to a point with the *same* spatial coordinates x^i at $t = dt$. Because of our freedom in assigning coordinates x^i to points on the time slices, it is possible that the second observer is not identical to the first observer, who was at rest in the slice. Let β^i/α denote the 3-velocity of the "coordinate observer" (observer at fixed x^i) relative to the "normal observer" (observer at rest in the slices). The quantity β^i is called the *shift vector*. The four quantities α and β^i correspond to the four degrees of freedom to make coordinate transformations in general relativity. In addition to evolution and initial-value equations for the metric, we will also have to prescribe how we wish to calculate α and β^i. This prescription is essentially arbitrary, but bad choices lead to unsatisfactory numerical solutions.

For example, if a black hole forms at the center of one's spatial grid, we know that in classical general relativity a singularity quickly appears there. This would halt any further numerical calculations. However, the black hole might have formed out of only a small fraction of the available matter. One might be interested in the further evolution of the matter outside the black hole, for example to study how much eventually accretes onto the hole. In such a case, one arranges that α gets small when the gravitational field gets large, but α stays close to unity in weak field regions. From equation (12), we see that such a prescription "holds back" proper time in the strong field region relative to the weak field region, postponing the appearance of the singularity.

The most commonly employed condition on α to achieve this goal is the *maximal slicing* condition. Geometrically, the slices are described by their intrinsic metric γ_{ij}, such that on the three-dimensional slice the line element is

$$^{(3)}ds^2 = \gamma_{ij} dx^i dx^j \, , \tag{13}$$

and by their *extrinsic curvature* K_{ij}, which describes how the slices are embedded in the four-dimensional spacetime. In terms of the variables already introduced, the mathematical definition of K_{ij} can be written as

$$-2\alpha K_{ij} = \partial_t \gamma_{ij} - \gamma_{ij,k}\beta^k - \gamma_{ik}\beta^k{}_{,j} - \gamma_{kj}\beta^k{}_{,i} \, . \tag{14}$$

Without the shift terms, this is conceptually the equation "velocity = ∂_t(coordinate)," with the metric γ_{ij} playing the role of the "coordinate." The equation "acceleration = ∂_t(velocity)" is the equation involving $\partial_t K_{ij}$. We will not need its explicit form here (cf. Smarr and York 1978*b*, eq. [3.6]). The equation is derived from the Gauss-Codazzi equations for embedding three-dimensional slices in a four-dimensional manifold. It involves the four-dimensional curvature, and it is here that physics takes over from geometry: the four-dimensional curvature is replaced by the stress-energy of matter according to Einstein's equations.

The maximal slicing condition is that $TrK_{ij} = K_i{}^i = 0$ for all time. Taking the trace of the equation for $\partial_t K_{ij}$, one finds an elliptic equation for α:

$$\Delta\alpha = \alpha[K_{ij}K^{ij} + 4\pi(\rho + S)] \, . \tag{15}$$

Here Δ denotes the covariant Laplacian on the time slice, while ρ and S are matter variables defined in terms of quantities measured by the normal observers:

$$\rho = T_{\mu\nu} n^\mu n^\nu = \text{total energy density} \, , \tag{16}$$

$$S = \gamma^{\mu\nu} T_{\mu\nu} = \gamma^{ij} T_{ij} = 3 \times \text{isotropic "pressure"} \, . \tag{17}$$

The vector n^μ is the normal to the time slices and $\gamma^{\mu\nu} \equiv g^{\mu\nu} + n^\mu n^\nu$. The normal has components

$$n_\mu = (-\alpha, 0, 0, 0) \, , \quad n^\mu = \frac{1}{\alpha}(1, -\beta^i) \, . \tag{18}$$

We adopt maximal slicing, as it has proved adequate for cases of spherical symmetry (Shapiro and Teukolsky 1979, 1980). Recently, there is some work suggesting that for nonspherical cases other slicing conditions may be preferable (Bardeen and Piran 1983; Stark and Piran 1985).

Our shift condition will be to make the spatial metric have a suitably simple form. We will choose this to be isotropic form, so that

$$^{(3)}ds^2 = A^2(dr^2 + r^2 d\theta^2 + r^2 \sin^2\theta d\phi^2) \, . \tag{19}$$

In spherical symmetry there is only one nonvanishing component β^r of β^i, so we will just call it β. In general, spherical symmetry requires *two* metric coefficients for the 3-metric:

$$^{(3)}ds^2 = A^2 dr^2 + B^2(r^2 d\theta^2 + r^2 \sin^2\theta d\phi^2) \, . \tag{20}$$

We are using the coordinate freedom to require that $A = B$. This leads to a condition on β, which we now determine.

If we write

$$K \equiv K^r{}_r = -2K^\theta{}_\theta = -2K^\phi{}_\phi \, , \tag{21}$$

we find from equation (14)

$$\beta = -\frac{3}{2} r \int_r^\infty \frac{\alpha K}{r} dr \, . \tag{22}$$

We also get an evolution equation for the metric coefficient A:

$$\partial_t A = \beta\left(\partial_r A + \frac{A}{r}\right) + \frac{1}{2}\alpha A K \, . \tag{23}$$

In spherical symmetry there is no gravitational radiation. This lack of gravitational dynamics shows mathematically by our being able to discard the equation for $\partial_t K_{ij}$. Instead, we get complete information about the metric on any slice from the *initial-value equations* for the gravitational field. As is well known, these are simply the four of Einstein's equations that have components along n^μ:

$$n^\mu n^\nu (G_{\mu\nu} - 8\pi T_{\mu\nu}) = 0 \, . \tag{24}$$

$$n^\mu \gamma^{\nu\lambda}(G_{\mu\lambda} - 8\pi T_{\mu\lambda}) = 0 \, . \tag{25}$$

Equation (24) is called the *Hamiltonian constraint* and reduces to

$$R - K_{ij}K^{ij} + (TrK)^2 = 16\pi\rho \, , \tag{26}$$

while the *momentum constraint* (25) reduces to

$$D^i(K_{ij} - \gamma_{ij} TrK) = -8\pi t_j \, . \tag{27}$$

Here R is the scalar curvature of the slice, D^i denotes a spatial covariant derivative, and the "momentum of the source" is

$$t_\alpha = n_\gamma \gamma_{\alpha\beta} T^{\beta\gamma} \, , \quad t_\alpha n^\alpha = 0 \, . \tag{28}$$

Equations (26) and (27) are initial-value equations because they

© American Astronomical Society • Provided by the NASA Astrophysics Data System

1985ApJ...298...34S

do not involve time derivatives. They are conceptually analogous to the divergence equations in Maxwell's equations.

For our case, the Hamiltonian constraint becomes

$$\frac{1}{r^2}\frac{\partial}{\partial r}\left(r^2\frac{\partial}{\partial r}A^{1/2}\right) = -\frac{1}{4}A^{5/2}\left(8\pi\rho + \frac{3}{4}K^2\right), \quad (29)$$

while the momentum constraint can be integrated with respect to r to give

$$K = \frac{-8\pi}{A^3 r^3}\int_0^r A^3 r^3 t_r\, dr\,. \quad (30)$$

The maximal slicing equation (15) for our case becomes

$$\frac{\partial}{\partial r}\left(Ar^2\frac{\partial}{\partial r}\alpha\right) = \alpha A^3 r^2\left(\frac{3}{2}K^2 + 8\pi\rho + 4\pi T\right). \quad (31)$$

Here we have replaced S by the trace of $T_{\alpha\beta}$, using the fact that

$$T = S - \rho\,. \quad (32)$$

c) Boundary Conditions

The boundary conditions on α, β, and A as $r\to\infty$ are that α and A tend to unity, while $\beta\to 0$. In numerical work, however, one wishes to impose the boundary conditions at a finite value of r outside the star. One relation comes from matching the metric (1) outside the star to the static Schwarzschild metric in isotropic coordinates:

$$ds^2 = -\frac{[1 - M/(2\bar{r})]^2}{[1 + M/(2\bar{r})]^2}dt_s^2 + \left(1 + \frac{M}{2r}\right)^4(d\bar{r}^2 + \bar{r}^2 d\theta^2 + \bar{r}^2\sin^2\theta d\phi^2)\,. \quad (33)$$

Here, $t_s = t_s(t, r)$ is the Schwarzschild time coordinate, and $\bar{r} = \bar{r}(t, r)$ is the isotropic radial coordinate.

The matching can be carried out by setting

$$dt_s = C(dt + Ddr)\,,$$
$$d\bar{r} = E(dt + Fdr)\,, \quad (34)$$

in equation (33). Here C, D, E, and F are functions of t and r. Equating the coefficients of the angular parts of (1) and (33) gives

$$\left(1 + \frac{M}{2r}\right)^2\bar{r} = Ar\,. \quad (35)$$

Equating coefficients of dt^2, $dtdr$, and dr^2 gives three relations between C, D, E, and F, and α, A, and β. However, note from equation (34) that

$$E = \frac{\partial\bar{r}}{\partial t}, \quad EF = \frac{\partial\bar{r}}{\partial r}\,. \quad (36)$$

These can be determined by differentiating equation (35). When we eliminate the remaining two quantities C and D from the three relations, we end up with a single relation among α, A, and β that must be satisfied outside the matter. After some algebra, we find that α and β drop out of the equation and we are left with

$$1 + r(\partial_r A)/A = [1 - 2M/(Ar) + r^2A^2K^2/4]^{1/2}\,. \quad (37)$$

Here we have used equation (23) to eliminate $A_{,t}$.

Since $K \approx 1/r^3$ as $r\to\infty$ (cf. eq. [30]), the approximate solution of equation (37) is

$$A = \left(1 + \frac{M}{2r}\right)^2\left[1 + 0\left(\frac{1}{r^4}\right)\right], \quad (38)$$

which is adequate for numerical work.

The reader can verify that

$$\alpha = 1 + r(\partial_r A)/A \quad (39)$$

is a solution of the maximal slicing equation (15) outside the star (substitute this expression in eq. [15] and use eq. [29] for $\partial_r{}^2A$). A second solution can be written down formally, since the maximal slicing equation is linear in α (cf., e.g., eq. [5.2.6] of Morse and Feshbach 1953). However, the only thing we learn from this is that the solution falls as $1/r$ at large r. Thus outside the matter we have

$$\alpha = 1 + r(\partial_r A)/A + \text{const.}\,[1/r + 0(1/r^2)]\,. \quad (40)$$

The constant is in principle determined by the boundary condition $\partial_r\alpha = 0$ at $r = 0$; in practice, we took the constant equal to zero and set the outer boundary at $r \gg M$.

The asymptotic solution of equation (22) gives

$$\beta = \tfrac{1}{2}rK[1 + 0(1/r)]\,. \quad (41)$$

The boundary conditions at the center of the star are that

$$0 = \partial_r\alpha = \partial_r A = \beta = K\,. \quad (42)$$

d) Source Terms

Substituting equations (2) and (18) in equation (16), we obtain for the source term ρ:

$$\rho = \sum_A m_A n_A(\alpha u_A^0)^2\,. \quad (43)$$

Regard each particle as being in its own category A, so that the sum over A is a sum over particles. Then

$$n_A = \frac{1}{\mathscr{V}_A} = \frac{1}{4\pi\alpha u_A^0 A^3 r^2\Delta r}\,. \quad (44)$$

Here $\mathscr{V}_A$ is the invariant (proper) 3-volume comoving with particle A. In the last equality in equation (44), we treat the particle as smeared out over a zone size Δr which is our spatial grid size.

Similarly, equation (28) gives for the source term in equation (30)

$$t_r = -\sum_A m_A n_A(\alpha u_A^0)u_{r(A)}\,, \quad (45)$$

while the trace of the stress-energy tensor that appears in equation (31) is

$$T = -\sum_A m_A n_A\,. \quad (46)$$

e) Diagnostics

An important check on the accuracy of a numerical scheme for integrating the dynamical equations given in this section is the conservation of the total mass-energy M. If we solve equation (37) for M, we find

$$M = \frac{1}{2}Ar\left[1 + \frac{1}{4}(ArK)^2 - \left(1 + \frac{r}{A}A_{,r}\right)^2\right]. \quad (47)$$

© American Astronomical Society • Provided by the NASA Astrophysics Data System

1985ApJ...298...34S

Our boundary condition (38) ensures that M stays constant at the outermost grid point, but one must check that equation (47) holds everywhere between the surface of the matter and the edge of the grid. An alternative derivation of equation (47) is to use the result of problem (16.10) of Lightman *et al.* (1975):

$$M = \left(\frac{\mathscr{A}}{16\pi}\right)^{1/2}\left(1 - \frac{\nabla\mathscr{A}\cdot\nabla\mathscr{A}}{16\pi}\right), \tag{48}$$

where

$$\mathscr{A} = 4\pi A^2 r^2 \tag{49}$$

is the proper area of the r = constant spheres.

A further check is available for stable, equilibrium clusters. Since the metric is static in such a case, each particle has a conserved energy, $E = -p_0$. Usually we just check the total "energy",

$$-E_0 \equiv \sum_A m_A u_0{}^A . \tag{50}$$

In cases where the cluster collapses, one would like to follow the growth of the black hole. We do this by calculating the trajectories of outgoing radial light rays emitted from various points. The null geodesic equation for the j^{th} ray is

$$\frac{dr_j}{dt} = \frac{\alpha(t, r_j)}{A(t, r_j)} - \beta(t, r_j) . \tag{51}$$

We map out the growth of the event horizon (surface of the black hole) by finding pairs of light rays emitted from the same radius at slightly different times, one of which escapes to infinity and one of which is pulled back into the black hole.

Inside a black hole there can be *trapped surfaces*, defined as regions where even an outgoing light ray immediately moves to a smaller radius. This condition is expressed by the equation

$$\frac{d\mathscr{A}}{dt} \le 0 , \tag{52}$$

where d/dt is the total derivative along the light ray. Using equations (49), (51), and (23), we find that condition (52) becomes

$$1 + r(\partial_r A)/A + ArK/2 \le 0 . \tag{53}$$

The *apparent horizon* is the outer boundary of the region of trapped surfaces. It occurs where equality holds in equations (52) and (53).

An important diagnostic for a star cluster is the *velocity distribution* of the stars. To determine this we must first specify the "mean rest frame" at each point. There is no unique way to do this, and we adopt the simple procedure of averaging the radial 4-velocities of all N_A particles in a given spatial zone:

$$U^r = \frac{1}{N_A}\sum_A u_A{}^r . \tag{54}$$

We then determine U^0 by the condition $\boldsymbol{U}\cdot\boldsymbol{U} = -1$. The basis vectors of an observer at rest in this frame are

$$\begin{aligned} \boldsymbol{e}_{\hat{0}} &= \boldsymbol{U} , \\ \boldsymbol{e}_{\hat{r}} &= \frac{1}{\alpha A}\left[(g_{rr}U^r + g_{0r}U^0)\boldsymbol{e}_0 - (g_{00}U^0 + g_{0r}U^r)\boldsymbol{e}_r\right] . \\ \boldsymbol{e}_{\hat{\theta}} &= \frac{1}{Ar}\boldsymbol{e}_\theta, \ \boldsymbol{e}_{\hat{\phi}} = \frac{1}{Ar}\boldsymbol{e}_\phi . \end{aligned} \tag{55}$$

Here $\boldsymbol{e}_{\hat{r}}$ has been determined by the orthonormality requirement.

The locally measured 3-velocity of a particle in this mean rest frame has radial component

$$v_A^{\hat{r}} = \frac{u_A^{\hat{r}}}{u_A^{\hat{0}}} = \frac{\boldsymbol{u}_A\cdot\boldsymbol{e}_{\hat{r}}}{-\boldsymbol{u}_A\cdot\boldsymbol{e}_{\hat{0}}} = \frac{\alpha A(U^0 u_A^r - U^r u_A^0)}{-(U_0 u_A^0 + U_r u_A^r)} . \tag{56}$$

Similarly,

$$v_A^{\hat{\phi}} = \frac{Aru_A^{\phi}}{-(U_0 u_A^0 + U_r u_A^r)} . \tag{57}$$

One can form averages of the components over a radial zone and calculate their dispersions ("temperatures"):

$$\begin{aligned} \langle v^{\hat{r}}\rangle &\equiv v^{\hat{r}} \equiv \frac{1}{N_A}\sum_A v_A^{\hat{r}} , \\ \langle (v^{\hat{r}})^2\rangle^{1/2} &\equiv v_{\text{rms}}^{\hat{r}} \equiv \frac{1}{N_A}\left[\sum_A (v_A^{\hat{r}} - v^{\hat{r}})^2\right]^{1/2} , \end{aligned} \tag{58}$$

and similarly for $\langle v^{\hat{\phi}}\rangle$ and $v_{\text{rms}}^{\hat{\phi}}$. (Note that $\langle v^{\hat{\phi}}\rangle = 0$ by assumption.) The *total* velocity dispersion satisfies

$$\langle v\rangle = [(v_{\text{rms}}^{\hat{r}})^2 + (v_{\text{rms}}^{\hat{\phi}})^2]^{1/2} \tag{59}$$

The velocity distribution is *isotropic* if

$$v_{\text{rms}}^{\hat{\phi}} = \sqrt{2}\, v_{\text{rms}}^{\hat{r}} . \tag{60}$$

A useful parameter that measures deviations from isotropy is the quantity

$$\mathscr{I} = \frac{v_{\text{rms}}^{\hat{r}} - v_{\text{rms}}^{\hat{\phi}}/2^{1/2}}{v_{\text{rms}}^{\hat{r}} + v_{\text{rms}}^{\hat{\phi}}/2^{1/2}} . \tag{61}$$

$\mathscr{I}$ is defined so that it equals 0 for isotropic (or dust) velocity dispersions, $+1$ for purely radial dispersions, and -1 for purely tangential dispersions.

IV. METHOD OF SOLUTION

a) Overview

Our numerical method for solving the Einstein equations for a collisionless system employs both finite difference and particle simulation techniques. The matter and matter current distributions, which serve as sources for the field equations, are determined by particle simulation. The metric fields are determined by solving one-dimensional, first- and second-order differential equations on each time slice. The first order equations (eqs. [22] and [30]) are solved by quadrature; the second order equations (eqs. [29] and [31]) are solved by finite differences on a discrete spatial grid.

A large number N_p of particles are chosen to represent the initial matter distribution. Their geodesic orbits are computed numerically on the assumption that the background metric field is spherically symmetric. During each time step the particles move in a "fixed" field background. This pseudo-linearization procedure temporarily decouples the matter evolution equations from the metric field equations. At regular time intervals, shorter than the minimum time scale for appreciable dynamical changes to occur, the "fixed" field is updated in response to the evolved matter and matter current distributions. In this fashion, a self-consistent field is maintained.

Because of spherical symmetry, each particle effectively represents an entire spherical shell of numerous "subparticles"

© American Astronomical Society • Provided by the NASA Astrophysics Data System

1985ApJ...298...34S

uniformly distributed over the the spherical area. Each subparticle on a given shell has the same rest mass, the same radial velocity u_r, the same transverse velocity u_ϕ, and a location at the same radial distance r from the center as all the other subparticles on the shell. Not only is each shell assumed to be spherically symmetric but, in addition, the distribution of the direction of the transverse velocities of its subparticles is isotropic. Accordingly, at each point on the shell, the directions of the transverse velocities for the different subparticles are uniformly distributed in the plane perpendicular to the radius vector. The general distribution function for such a configuration then depends only on the three phase space variables r, p_r, and p_ϕ and time t: $f = f(r, p_r, p_\phi, t)$.

We take each of the N_p particles (or shells) to have equal rest mass $m_0 \equiv M_0/N_p$, where M_0 is the total *rest* mass of the system. This simplification is by no means essential, since the rest masses of collisionless particles do not enter the fundamental dynamical equations of motion or the field equations ("Equivalence Principle"). Indeed, we have even experimented crudely with assigning unequal position-dependent rest masses to the particles to obtain greater statistical coverage in sparsely populated regions of phase space. This "mass renormalization" procedure seems to work well when there is no shell crossing (e.g., Oppenheimer-Synder dust collapse). However, the method, in its simplest form, still yields appreciable statistical fluctuations (unless N is extremely large) whenever, as is typically the case, shell crossing occurs. Hence our generic code assigns equal rest masses to the particles.

b) *The Logical Flow*

It would be inappropriate for us to present our numerical code (which consists of approximately 3000 lines of FORTRAN broken up into 57 subroutines) in full detail here. Instead, we shall restrict our discussion to a short summary of some of the salient features of our numerical algorithms and a brief sketch of the code's logical flow (see Fig. 1).

The essence of our code is the manner in which it evolves the matter and field variables from one time slice at t to the next time slice at $t + \Delta t$. The N_p particles, which determine the matter distribution, are evolved forward in time by integrating the geodesic equations (8) and (9) for $r_j(t + \Delta t)$ and $u_{rj}(t + \Delta t)$, where $1 \le j \le N_p$. The integrations in the "fixed" field background are performed via a fourth order Runge-Kutta scheme with an adaptive time-step size. The "forces" appearing on the right-hand sides of the geodesic equations are calculated from the "fixed" metric field components. These field components are stored on a discrete, isotropic, radial coordinate grid r_i, $1 \le i \le N_f$, which covers the spatial hypersurface from the origin at $r = 0$ out to some fixed, distant radius $r = r_{\max}(\gg M)$ residing outside the matter distribution in the exterior vacuum. The "forces," computed numerically from these stored metric coefficients, are also stored as the grid points r_i, where they are held fixed until the metric is updated. In solving the geodesic equation, the local value of the instantaneous "force" on a particle at radius r_j is interpolated (to second order in accuracy) from the values stored on the grid points r_i.

Once all the particles have been evolved to the new time slice at $t + \Delta t$, they are sorted in order of increasing radius r_j. Sorting facilitates the construction of a new radial coordinate grid r_i on the new spatial hypersurface. The radial grid is designed to fulfill *two* distinct (and not always compatible) functions. First, the grid must provide "good coverage" of the particle distribution, so that when the particles are binned on the mesh, they yield a statistically reliable representation of the matter and matter current distributions everywhere. Thus we must "put the grid points where the particles are." Second, the grid must be meshed sufficiently finely and uniformly (at least locally), so that the field variables can be accurately determined on the mesh by quadrature (eqs. [22] and [30]) or finite differencing (eqs. [29] and [31]). It must also extend out sufficiently far into the exterior vacuum ($r_{\max} \gg M$), so that the asymptotic outer boundary conditions on the field variables can be imposed reliably.

In constructing our grid to fulfill these two different requirements, we strike a compromise. The grid is essentially Eulerian, but in order to accommodate the requirement of "good particle coverage," our zoning algorithm imparts a mixed Eulerian-Lagrangian character to the mesh. Specifically, we split the grid into two parts: we have an *interior* grid which covers the matter and extends from $0 \le r \le r_{j=N_p}$ (the outermost particle radius), and an *exterior* grid which resides in the exterior vacuum and extends from $r_{j=N_p} \le r \le r_{\max}$. The first zone is forced to follow a fixed number of particles (i.e., a fixed fraction of the rest mass) at all times. By alloting a fixed number of zones to the region containing matter and by following a fixed rest mass fraction, at least in the all-important central regions, we guarantee reasonably good coverage at all times. Successive interior zones are constructed by geometric series to have widths $(\Delta r_i)^3$ (where $[\Delta r_i]^3$ is proportional to coordinate "volume") which vary by a constant ratio, near unity, at any given time (the ratio changing from time slice to time slice as the matter moves). This procedure yields a mesh which, at least locally, is nearly equally spaced in coordinate volume, thereby facilitating second-order accurate integration of the field equations. The exterior grid joins smoothly onto the interior at $r_{j=N_p}$ and at all times extends out to $r_{\max}$. It is also constructed by geometric series to have adjacent zones with radial widths which vary by a constant ratio near unity at any given time. This again facilitates second-order accurate integrations out to the outer boundary at $r_{\max}$.

Following particle sorting and grid rezoning at $t + \Delta t$, particles are binned in order to compute the smoothed matter source terms t_r, T, and ρ for the field equations (29)–(31). The field quantities A, α, β, and K are then calculated on the grid points overlaying the new spatial hypersurface. Care is needed in handling the nonlinearities in A in the Hamiltonian equation (29). We make a first guess for A on the new time slice by integrating the evolution equation (23) from t to $t + \Delta t$ and then refine this value by linearizing and iterating equation (29); cf. Shapiro and Teukolsky (1980). Essentially, we are solving an initial-value problem for the metric at each time slice, so that the metric corresponds to the instantaneous matter distribution to high accuracy. (Direct solution of the evolution eq. [23] is less accurate). Following linearization and finite differencing, the Hamiltonian constraint equation becomes a tridiagonal matrix equation for A and is easily solved by standard techniques and then iterated until convergence is achieved. The maximal slicing equation (31) for α is linear; following finite differencing it also yields a tridiagonal matrix equation which can be simply solved. The equations for K and β are solved by quadrature.

Once the new field quantities have been calculated, the positions $r_{L,k}$ of the outgoing radial light rays are determined in the new time slice by integrating the null geodesic equation (51) from t to $t + \Delta t$. These rays act as diagnostic probes of the

© American Astronomical Society • Provided by the NASA Astrophysics Data System

1985ApJ...298...34S

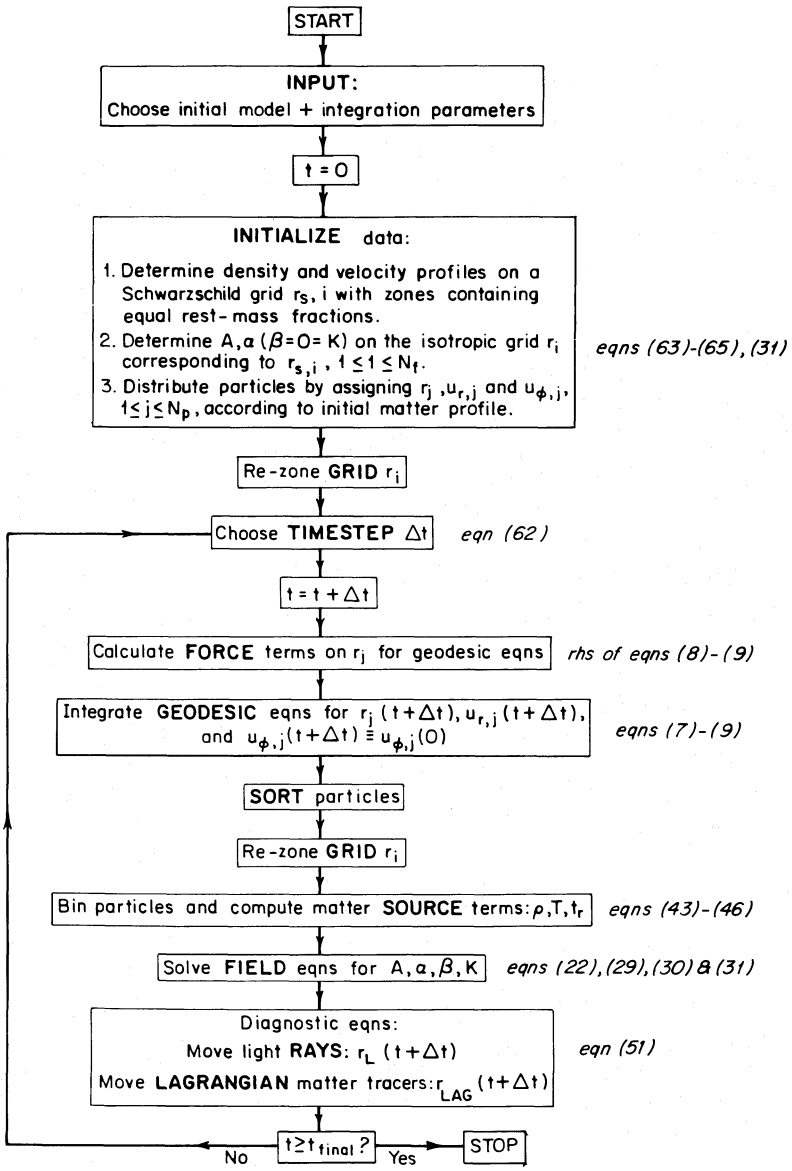

FIG. 1.—Logical flowchart of numerical method

spacetime geometry and serve to identify the existence of an event horizon in the case of black hole formation.

Printout, provided at regular intervals, displays the metric fields and matter source profiles on a time slice as well as the matter velocity and velocity dispersion profiles, rest mass fraction, and rest density and particle number profiles. Other diagnostics printed out on each time slice include the global energy diagnostic integral (eq. [50]), the region of trapped surfaces (if any exist), and M, the total mass-energy of the interior as derived from the exterior metric via equation (47). At the end of the computations, the world lines of fictitious Lagrangian matter tracers situated at radii containing fixed fractions of the interior rest mass are retrieved from storage and tabulated together with the null ray trajectories. It is sometimes very instructive to project the entire "stellar" image of a cluster onto a color graphics monitor to follow the orbital motions of the N_p particles (tabulating all N_p particle positions as a function of time is quite unwieldy when $N_p \ge 1000$). Individual particle position data, the null ray trajectories, and α profiles are stored at every time step and can be retrieved to provide color still images and motion picture films of an evolving cluster, as desired.

The time step Δt during which the metric fields and "force" terms are held fixed must be sufficiently small that the matter distribution changes by only a small fractional amount. We take as a conservative measure of the local time scale for appreciable dynamical changes the proper time for the collapse to a singularity of a spherical, homogeneous, cold dust ball, initially at rest, with total mass-energy density ρ equal to the local value. Accordingly, we set

$$\Delta t = q\left(\frac{3\pi}{32\rho_{\max}}\right)^{1/2}, \quad \rho_{\max} = \max\{\rho_i\}, \quad 1 \le i \le N_f. \quad (62)$$

Here $\rho_{\max}$ is the maximum mass-energy density in the cluster and $q \lesssim 0.1$ is a constant accuracy parameter less than unity chosen at the beginning of the computation.

© American Astronomical Society • Provided by the NASA Astrophysics Data System

1985ApJ...298...34S

V. INITIAL DATA

a) Method of Preparation

Preparation of the initial data is one of the most crucial aspects of our numerical code. Our ability to assess the outcome of various dynamical scenarios is limited by, among other factors, the accuracy with which we can represent a chosen initial configuration by discrete metric and matter data on the initial spatial lattice. Indeed, the reliability of our numerical spacetimes is only as good as the numerical accuracy of our initial spatial hypersurface.

Our preparation of initial data begins by placing the density and velocity profiles of a chosen matter distribution on a *Schwarzschild* (*areal*) radial grid, $r_{s,i}$. The initial configuration is assumed to be momentarily static, i.e., the initial time slice at $t = 0$ is taken to be a moment of time symmetry. The Schwarzschild radial grid consists of zones of equal rest mass, which facilitates an "equitable" placement of particles on the mesh later in the initialization process. The choice of an initial time-symmetric cluster model is quite arbitary but is typically performed in one of two ways. For some models we specify the matter and velocity profiles on $r_{s,i}$ immediately, as they are sufficiently simple and essentially analytic (e.g., a homogeneous spherical cluster of particles all moving on circular orbits). For other models we specify an isotropic particle phase-space distribution function, $f = f(E)$, where $E = -p_0$ is the "energy at infinity" of star. For a chosen $f(E)$, the equilibrium equations of structure for a spherical system (see Misner, Thorne, and Wheeler 1973, § 25.7) are then integrated to determine the density and velocity profiles on $r_{s,i}$.

Once the density and velocity profiles are known on $r_{s,i}$, the *isotropic* radial coordinates r_i corresponding to $r_{s,i}$, together with the isotropic conformal metric factor $A(r_i)$ can be determined by integrating the familiar equation of mass-energy (i.e., the Hamiltonian constraint equation in Schwarzschild coordinates at a moment of time symmetry)

$$\frac{dm(r_s)}{dr_s} = 4\pi r_s{}^2 \rho(r_s) \; ; \quad m(0) = 0 \text{ at } r_s = 0 \, , \tag{63}$$

simultaneously with the coordinate transformation equations

$$\frac{dr}{dr_s} = \frac{(r/r_s)}{[1 - 2m(r_s)/r_s]^{1/2}} \, , \quad r_s < R \, , \tag{64}$$

$$r = \tfrac{1}{2}\{r_s - M + [r_s(r_s - 2M)]^{1/2}\} \, , \quad r_s > R \, ,$$

$$A(r) = r_s/r \, . \tag{65}$$

Here $r_s = R$ is the Schwarzschild coordinate of the matter surface. Next, equation (31) for $\alpha(r_i)$ is solved by finite-differencing on r_i, where $\beta(r_i) = 0 = K(r_i)$ by time symmetry. Discrete matter and metric field profiles now reside on an isotropic radial grid which in the interior has zones containing equal rest mass fractions. These profiles are printed out.

Next, the particles are distributed throughout the interior isotropic zones with isotropic radial positions r_j and velocities $u_{r,j}$ and $u_{\phi,j}$, $1 \le j \le N_p$ in accord with the rest-mass and velocity profiles computed above. Once the particle positions and velocities have been assigned, the isotropic mesh is rezoned in the manner described in § IV*b*. Though no longer a grid with zones containing equal rest mass (i.e., equal particle number), the new isotropic grid (1) is nearly uniform in rest mass, at least at the center where $\rho_0 \approx$ constant, and (2) is better suited to solving the α and A equations (31) and (29) by finite differencing. As a check on our entire particle-field initialization procedure, we recalculate the smooth density, velocity, and all other matter profiles by binning the particles and adding up their individual contributions. We thereby redetermine the initial matter source terms for the field quantities from the particle data in the same way these source terms are determined on all future time slices $t > 0$. These source terms are then used to redetermine the metric coefficients according to the same finite-difference prescription employed at all subsequent times. This redundant set of discrete matter and metric field profiles based on the new isotropic grid and the *discrete* particle data is printed out and compared with the previous output, derived from continuous profile functions [e.g., $f(E)$]. This comparison provides crucial verification of our particle distribution routines, choice and extent of radial zoning, and field intergration algorithms *before* we proceed to evolve the data into the future. In particular, it helps us assess and subsequently control the degree of statistical fluctuations in our discrete profiles resulting from sampling a continuous profile with only a *finite* number of particles.

b) The Menu at a Glance

We consider two broad categories of initial data: "circular orbit" clusters and "isotropic orbit" clusters. The former category includes all clusters whose particles move strictly in tangential (i.e., radially transverse) trajectories initially. The latter category focuses on clusters whose initial particle distributions are specified by a distribution function of the form $f(E)$. Circular orbit clusters, which include "cold" clusters whose particles are initially at rest, are particularly useful in performing test-bed calculations. Equilibrium models, stability criteria, and even complete dynamical solutions for special cases (e.g., homogeneous dust collapse—a "slice of the Friedmann universe") can be determined in advance essentially analytically. These results can then be used to check the code (see § VI). Isotropic orbit clusters provide the basis for addressing most of the interesting, physically relevant questions concerning the evolution of more realistic relativistic systems.

VI. TEST-BED CALCULATIONS

We have performed a very intensive and systematic battery of test-bed calculations to evaluate the overall performance of our numerical scheme. These calculations, summarized in Table 1, were carefully constructed to test the ability of our numerical code to reproduce previously known "analytic" results. (Here "analytic" refers to all computations which do not require the solution of partial differential equations; e.g., numerical solutions of ordinary differential equations qualify as "analytic.") Such previous results range from full solutions of dynamical spacetimes, as in the case of Oppenheimer-Snyder collapse to a black hole or static models of stable, equilibrium configurations, to the identification of unstable models along an equilibrium sequence as gleaned from linear perturbation theory. Our test simulations of cases falling into the latter category are of particular physical significance, since the nonlinear growth of these instabilities and the final fates of these unstable configurations has been heretofore unknown. We focus on these cases in Paper II.

The modular construction of our code facilited a "hierarchical" testing program, whereby the least complicated tests, which called only some of our subroutines, could be performed first, while the most complicated tests, which utilized all the subroutines, could be performed last. This pro-

© American Astronomical Society • Provided by the NASA Astrophysics Data System

1985ApJ...298...34S

TABLE 1

TEST-BED CALCULATIONS

CASE	CHARACTERIZATION	FIELD STATUS	ALGORITHMS ACTIVATED[a]	TESTS PASSED	
				Matter Quantities	Metric Fields
1.....	Radial and circular test particle orbits in Schwarzschild geometry	Fixed	FORCE, GEODESIC	Orbits maintained analytic trajectories; located last stable circular orbit at $r_s = 6M$; p_t conserved	None
2[b].....	Monoenergetic, isotropic equilibrium test particle distribution in Schwarzschild geometry	Fixed	FORCE, GEODESIC, SOURCE	Density and velocity profiles maintained analytic equilibrium values; p_t and E_0 conserved	None
3[c].....	Test particle motion in initially self-consistent equilibrium field	Fixed	All	Density and velocity profiles maintained equilibrium values; p_t and E_0 conserved	None
4[d].....	Homogeneous dust collapse (Oppenheimer-Snyder)	Dynamic	All	Density and velocity profiles reproduced analytic solution in maximal gauge	Metric profiles reproduced analytic values in maximal gauge; limit surface located accurately; accurate formation of black hole event horizon and trapped surface
5[d].....	Homogeneous equilibrium clusters (circular orbits)	Dynamic	All	Density and circular velocity profiles maintained equilibrium values for $R/M > 6$; p_t and E_0 conserved; found instability for $4 < R/M < 6$	Metric profile maintained equilibrium interior and vacuum Schwarzschild exterior values for $R/M > 6$
6[e].....	Homogeneous nonequilibrium clusters (tangential orbits initially)	Dynamic	All	Located critical, analytic value of v^{ϕ} separating collapse and bounce from collapse to black hole	Accurate formation of black hole event horizon and trapped surface
7[f].....	Newtonian homogeneous nonequilibrium clusters (tangential orbits initially)	Dynamic	All	Reproduced analytic homologous oscillation solution; preserved homogeneous density and linear velocity profiles and found correct period; $E_{\rm Newt}$ conserved	Reproduced analytic quadratic potential field
8[g].....	Parabolic equilibrium clusters (circular orbits)	Dynamic	All	Density and circular velocity profiles maintained equilibrium values for $R/M > 6.25$; p_t and E_0 conserved; found instability for $3.125 < R/M < 6.25$	Metric profiles maintained equilibrium interior and vacuum Schwarzschild exterior values for $R/M > 6.25$
9.....	Parabolic nonequilibrium clusters (tangential orbits initially)	Dynamic	All	Similar to case 6	
10[h].....	Maxwell-Boltzmann equilibrium clusters	Dynamic	All	Density and velocity profiles maintained equilibrium values; p_t and E_0 conserved for stable models; unstable ($\omega^2 < 0$) Ipser 1969*b* models collapsed to black holes	Metric profiles maintained equilibrium interior and vacuum Schwarzschild exterior values for stable models; accurate formation of black hole event horizon and trapped surface for unstable models
11[h].....	Monoenergetic equilibrium clusters	Dynamic	All	Similar to case 10	

© American Astronomical Society • Provided by the NASA Astrophysics Data System

1985ApJ...298...34S

TABLE 1 (*cont.*)

Case	Characterization	Field Status	Algorithms Activated[a]	Tests Passed: Matter Quantities	Tests Passed: Metric Fields
12[h].....	Power-law equilibrium clusters	Dynamic	All	Similar to case 10	
13[h].....	Newtonian power-law equilibrium clusters (including polytropes)	Dynamic	All	Density and velocity profiles maintained equilibrium values; $E_{\rm Newt}$ conserved and virial theorem obeyed. All permitted polytropes ($\frac{1}{2} < n < \infty$) maintained stable equilibrium, in accord with Antonov 1962, Lynden-Bell and Sanitt 1969, and Henon 1973.	Maintained polytropic potential field
14[h].....	Relativistic $n = 4$ polytropes	Dynamic	All	Similar to Case 10 Unstable ($\omega^2 < 0$) Fackerell 1970 models collapsed to balck holes	

[a] Operative routines are: INITIALIZE, TIMESTEP, FORCE, GEODESIC, SORT, GRID, SOURCE, FIELD, RAY, LAGRANGIAN; see Fig. 1 and § V for a description.
[b] See Appendix A.
[c] The fixed metric field and *initial* test particle distribution correspond to a stable, equilibrium configuration obeying a truncated Maxwell-Boltzmann distribution function.
[d] See § VII*b*.
[e] See Appendix B and Paper II.
[f] See Appendix C.
[g] See Appendix D.
[h] See Paper II.

cedure was crucial in identifying subunits of our code responsible for any bugs, inaccuracies, or general inefficiencies. The order in which the various calculations were performed is indicated roughly by the order in which they appear in Table 1.

Two broad classes of test-bed calculations were performed: fixed-field calculations, in which the matter moved in a fixed background metric field, and dynamic-field calculations, in which the background field was updated regularly to maintain self-consistency with the evolving matter profile. Details of these calculations are summarized in Table 1, § VII, and Appendicies A–D, and in Paper II.

Our test-bed calculations explore a very broad variety of initial configurations. They range from completely isotropic to highly anisotropic (i.e., tangential orbits), homogeneous to very centrally condensed (i.e., extreme "core-halo" configurations), very relativistic to Newtonian (potential $\Phi \ll 1$, $v^2 \ll 1$). This variety enables us to test the full dynamic range of our numerical scheme and to address a large physical range of issues concerning the dynamical behavior of spherical, collisionless gases in general relativity.

VII. SAMPLE OF NUMERICAL RESULTS

a) Homogeneous Dust Collapse

The dynamical evolution of a homogeneous dust ball, initially at rest, provides a stringent test of the ability of our code to follow the collapse of a collisionless system to a black hole. The initial configuration is specified uniquely by its nondimensional radius R/M, where R is the Schwarzschild radial coordinate of the surface and M the total mass-energy of the sphere. The corresponding mass-energy density profile is given by

$$\rho(r_s) = \begin{cases} \dfrac{3M}{4\pi R^3}, & 0 \le r_s \le R, \quad (66) \\ 0, & r_s > R. \quad (67) \end{cases}$$

All particle velocities are initially zero.

The subsequent dynamical behavior is given by the interior solution of a closed Friedmann universe matched smoothly onto an exterior Schwarzschild vacuum. The evolution consists of spherical collapse to a Schwarzschild black hole, beginning at a moment of time symmetry (i.e., the instant of "maximum expansion" in closed Friedmann evolution). This dynamical solution is known analytically (Oppenheimer and Snyder 1939) and can be expressed in closed form in the usual Friedmann comoving, *synchronous* coordinate system. In a synchronous gauge, we have $\alpha \equiv 1$ and $\beta \equiv 0$ for all $t \ge 0$. Moreover, collapse to a singularity occurs in a finite *coordinate* time $\Delta t = (3\pi/32\rho)^{1/2}$, where ρ is given by equation (66). Recall that collapse to a black hole is always accompanied by the formation of singularities in a finite *proper* time (Hawking and Ellis 1973), but in a synchronous gauge we have coordinate time the same as proper time throughout the matter. Our numerical scheme, however, is by design based on the *maximal* gauge, with $\alpha \neq 1$. Choosing maximal time slicing conveniently postpones the formation of singularities until far into the future ($t \to \infty$). However, one is forced to transform the exact Friedmann solution, expressible in closed form in synchronous

© American Astronomical Society • Provided by the NASA Astrophysics Data System

1985ApJ...298...34S

coordinates, to the maximal coordinate system in order to evaluate the computer generated spacetime. This coordinate transformation is essentially "analytic" in that it requires the solution of ordinary differential equations on a given maximal time slice. The transformation of some of the relevant quantities was originally performed by Eardley and Smarr (1979). The complete solution for homogeneous dust collapse in a maximal gauge has been obtained more recently by Petrich, Shapiro, and Teukolsky (1985, hereafter PST).

In Figures 2–9 we compare the "exact" results of PST with the computer-generated spacetimes obtained with the collisionless particle code presented here. The case illustrated is for $R/M = 10$ at $t = 0$. For these comparisons we selected a modest set of integration accuracy parameters for running our code. For example, we employed $N_s = 240$ radial grid points to compute the metric field quantities. Of these, only 60 were used to cover the interior of the matter distribution, with the rest residing in the vacuum exterior at all times. The outer boundary was fixed at $r_{max}/M = 100$. The total number of particles tracked was $N_p = 1180$. The timestep parameter for field updates q appearing in equation (62) was fixed at $q = 0.05$. The collapse was followed for a total of 331 time step loops (i.e., field updates), as depicted in Figure 1. The code was run on an FPS 164 Array Processor, hosted by an IBM 3081. For this case the total integration time was ~ 1.5 CPU hr.

The resulting metric field profiles during the collapse are plotted in Figures 2, 3, and 4 on selected maximal hypersurfaces labeled by t/M. Solid lines give the exact PST values, while circles show the corresponding computer-generated points. The chosen spatial hypersurfaces on which the two sets of data are compared was actually specified by α_i, the central value of the lapse. The corresponding values of t/M for the two sets differed somewhat, but only by a percent or so. This small time offset is established during the first few time step loops, when ρ_{max} is small and Δt is relatively large (cf. eq. [62]); the offset remains constant thereafter. The offset can be reduced arbitrarily by choosing arbitrarily small values of q. By experimentation, we find that reducing q by $\frac{1}{2}$ reduces the fractional time offset by approximately the same amount while doubling the total required integration (CPU) time. The results depicted represent a fair attempt at obtaining high accuracy with modest integration time.

It is clear from Figures 2–4 that the metric profiles generated by our code are extremely accurate. Not only is the exponential "collapse of lapse" of α_i with time evident (see, e.g., York 1979 and PST for an extensive discussion) together with the accompanying growth of the spatial metric component A and shift vector β, but, more significantly, the actual numerical values of these metric coefficients remain remarkably close to the exact answers. This statement applies not just to the initial few time slices but equally well to late times, long after the appearance of an event horizon and trapped surface (see below). By reproducing exact profiles accurate over many decades, the code exhibits appreciable dynamic range. The accuracy of the results obtained here with a collisionless particle simulation code far exceeds the accuracy of typical relativistic spherical hydrodynamic codes (see, e.g., Shapiro and Teukolsky 1980) for dust collapse, especially at late times. This is presumably due to the fact that when a gas is collisionless, it is more accurate to follow the matter by integrating ordinary differential geodesic equations then partial differential hydrodynamic equations. (Of course, dust or "cold" matter evolution represents essentially the only case in which the two gas prescriptions—collisionless and hydrodynamic—are equally applicable.)

Corresponding matter profiles on selected time slices are plotted in Figures 5–7. The total mass-energy density $\rho = \boldsymbol{n} \cdot \boldsymbol{T} \cdot \boldsymbol{n}$ and rest-mass density $\rho_0 = \boldsymbol{n} \cdot \boldsymbol{T} \cdot \boldsymbol{u}$, as mea-

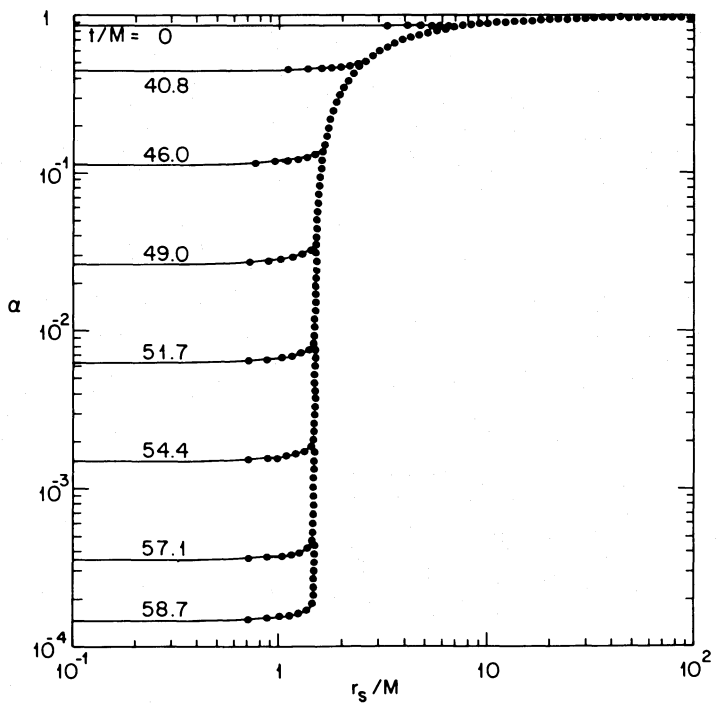

FIG. 2.—The lapse function α as a function of areal radius r_s on selected time slices for Oppenheimer-Snyder collapse from $R = 10M$. The solid lines are the results of exact integrations by PST. The dots are the results obtained with the method reported here. See text for further details.

© American Astronomical Society • Provided by the NASA Astrophysics Data System

1985ApJ...298...34S

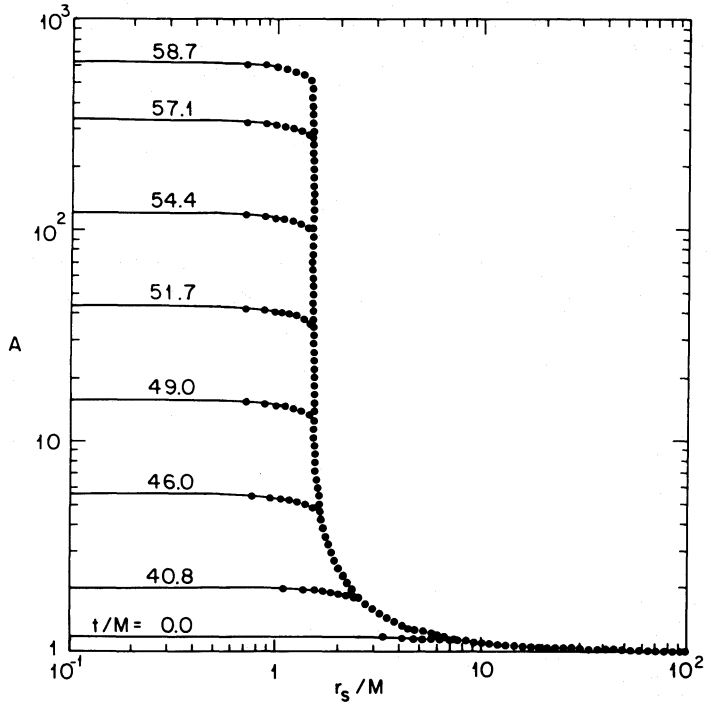

FIG. 3.—The metric component A as a function of areal radius r_s for the case described in Fig. 2

sured by a *normal* observer $\boldsymbol{n}$, are plotted in Figures 5 and 6 respectively. Here $\boldsymbol{u}$ is the velocity 4-vector of the fluid, while

$$\boldsymbol{T} = \rho_* \boldsymbol{u} \times \boldsymbol{u} \tag{68}$$

is the stress-energy tensor and ρ_* is the rest density in a *comoving* frame with 4-velocity $\boldsymbol{u}$. The radial velocity

$$\frac{dr}{dt} = \frac{u^r}{u^0} \tag{69}$$

is plotted in Figure 7. Now in comoving, synchronous coordinates, $\boldsymbol{n} = \boldsymbol{u}$; hence $\rho = \rho_0 = \rho_*$ in this gauge. Moreover, the densities remain homogeneous with advancing (proper) time. In maximal time slicing, the lapse α holds back the advance of proper time near the center, i.e., as t increases, proper time advances more slowly at the center, where α is smallest, than at the surface, where α is larger. Hence the densities are larger at the surface than at the center. Again, the agreement between the exact and the computer-generated solution is quite good.

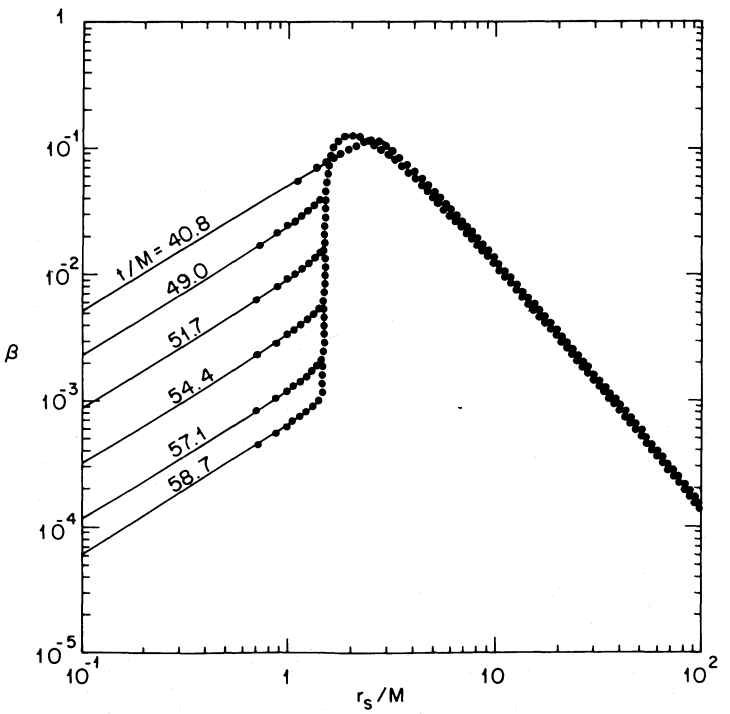

FIG. 4.—The shift β as a function of areal radius r_s for the case described in Fig. 2

© American Astronomical Society • Provided by the NASA Astrophysics Data System

1985ApJ...298...34S

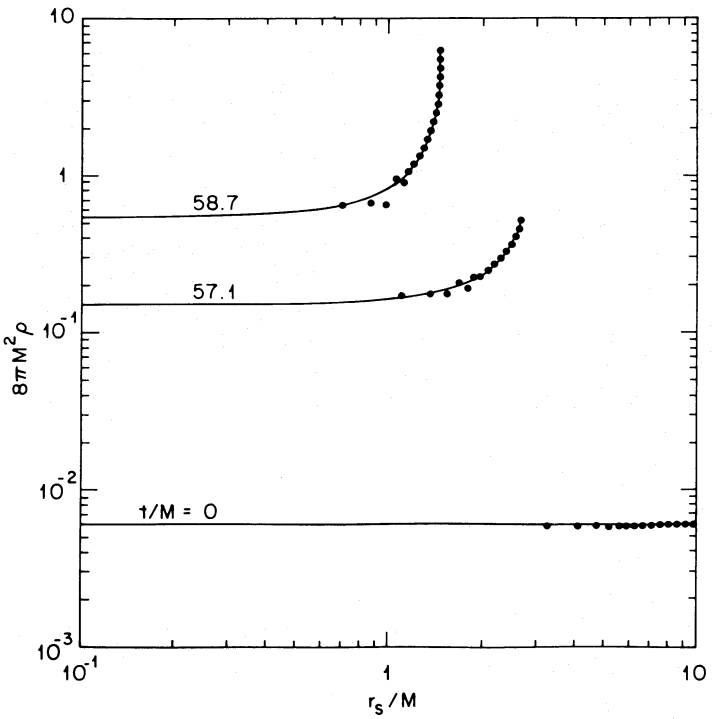

FIG. 5.—The total mass-energy density ρ as measured by a normal observer for the case described in Fig. 2. At $t = 0$ the configuration is homogeneous.

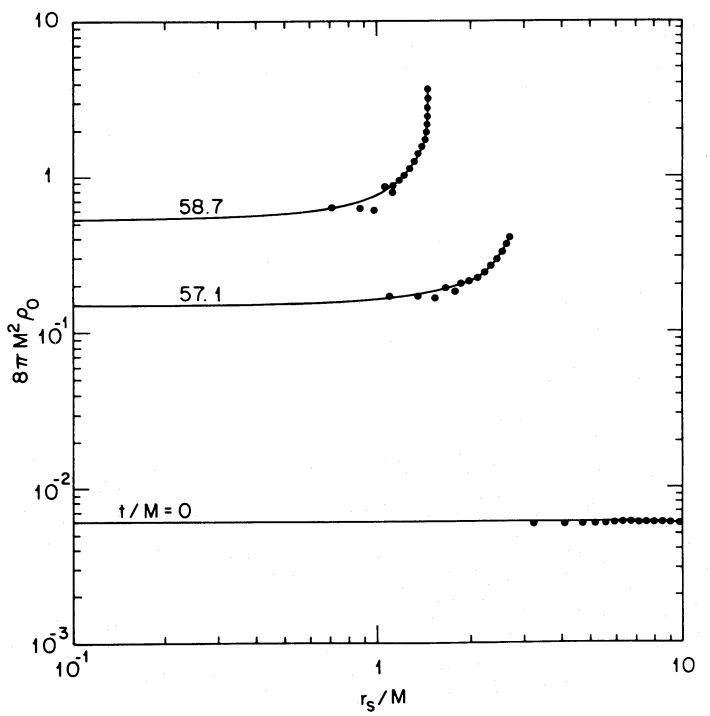

FIG. 6.—The rest-mass density ρ_0 as measured by a normal observer for the case described in Fig. 2. At $t = 0$, $\rho_0 = \rho$.

© American Astronomical Society • Provided by the NASA Astrophysics Data System

1985ApJ...298...34S

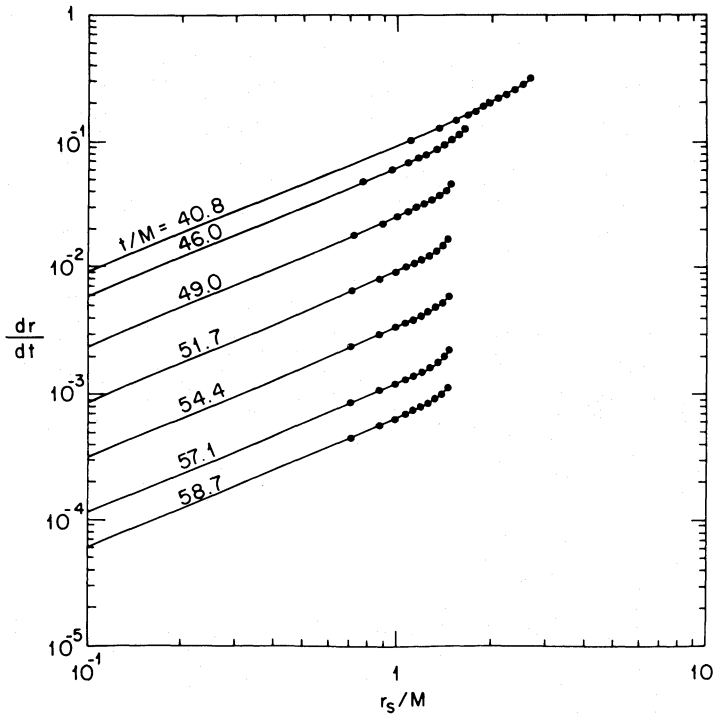

FIG. 7.—The inward radial velocity dr/dt for the case described in Fig. 2. At $t = 0$, dr/dt is everywhere zero.

In Figure 8 we plot the world lines of fictitious Lagrangian matter tracers in a spacetime diagram. In Figure 9 we zoom in on the region near the center at late times to analyze the formation and growth of the central black hole. The smooth dotted lines show the exact trajectories of the particles, while the heavy dots give the computer-generated values. The dashed line shows the event horizon found from the exact solution. Outward radial light rays emitted from inside the event horizon can never escape to infinity but must eventually fall back toward the center. The shaded region represents the region of trapped surfaces, where even an outgoing spherical flash of light immediately propagates to a sphere of smaller area.

The computer-generated spacetime diagram is in excellent agreement with the exact results. In particular, the particle world lines follow the exact trajectories reasonably closely; only the small initial time "offset" discussed above prevents perfect coincidence (the choice of a smaller integration parameter q considerably reduces the residual discrepancy, which seems to vary linearly with q). The steep vertical rise in the world lines at late times is due to the appearance of a "limit surface" in the maximal gauge (Eardley and Smarr 1979; PST), which is the minimum radius that the matter surface asymptotically approaches as $t \to \infty$ with maximal slicing. For $R/M = 10$ at $t = 0$, the "limit" surface forms at $r_s/M = 1.474$ in the exact solution and at $r_s/M = 1.47$ in the computer-generated one.

The particle simulation code can probe the spacetime geometry quite accurately, even for modest choices of integration accuracy parameters. For example, according to the exact solution, the region of trapped surfaces first appears precisely on the 2-sphere at $r_s/M \equiv 2$, after which the apparent horizon (outermost trapped surface) remains at $r_s/M \equiv 2$ while the innermost rapped surface moves inward, asymptotically reaching $r_s/M = 1.45(2)$ at late times (see Fig. 9). By employing equation (53) to locate the trapped surfaces in the computer-generated spacetime, we find that the apparent horizon first forms and remains close to $r_s/M = 1.97$, while the inner horizon asymptotically reaches $r_s/M = 1.45$ at late times. This numerical agreement is quite good, which is not surprising given the excellent match found for the metric profiles. We find that even these discrepancies can be made arbitrarily small with a more stringent selection of integration accuracy parameters. We thus have reasonable confidence that our scheme is reliable and numerically stable.

We further probe the spacetime geometry by emitting outgoing radial light rays near the center at various times. By finding pairs of rays emitted from the same radius, one of which escapes and one of which does not, we can trace the growth of the event horizon as more and more matter flows into the black hole. Determined in this way, the event horizon lies very close to the exact result plotted in Figures 8 and 9. In particular, (1) the event horizon first appears at the center and grows monotonically outward to $r_s/M = 2.0$, and (2) the apparent horizon always lies inside the event horizon and asymptotically approaches it at late times. These results are in accordance with rigorous theorems on black holes (Hawking and Ellis 1973).

By late times *all* the matter is well inside the event horizon (see Fig. 9). By employing equation (47), we find that the total interior mass-energy M, inferred from the computed metric coefficients, is constant throughout the exterior and equal to its initial value to within 1%. This result provides a powerful global check on our code. It guarantees that our particle sample size, geodesic integrations, and binning algorithms were all adequate to determine the matter source terms accurately, and that our numerical integrations of the metric field equations were quite reliable.

We terminate our computer integrations when the central lapse α_c falls to 1.5×10^{-4}. This value gives $\Delta\tau_c/\Delta t$, the ratio of

© American Astronomical Society • Provided by the NASA Astrophysics Data System

1985ApJ...298...34S

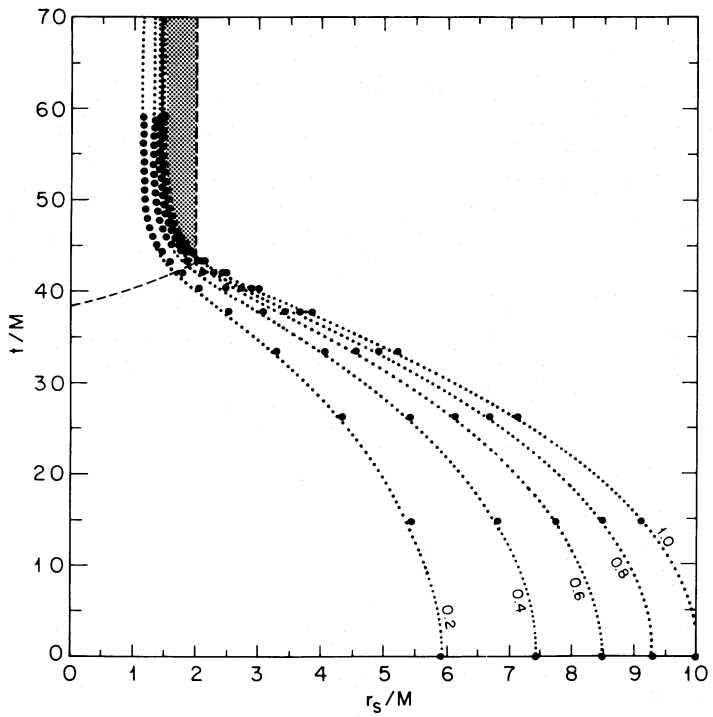

FIG. 8.—Spacetime diagram for Oppenheimer-Snyder collapse from $R = 10M$. The dotted lines are the world lines of Lagrangian matter elements from the exact integrations of PST. Each world line is labeled by the fixed interior rest mass fraction. The dots are points for the corresponding matter elements obtained with the method of this paper. The dashed line is the event horizon. The shaded area is the region of trapped surfaces. Its outer boundary, the apparent horizon, coincides with the event horizon. Its inner boundary is just inside the surface of the matter.

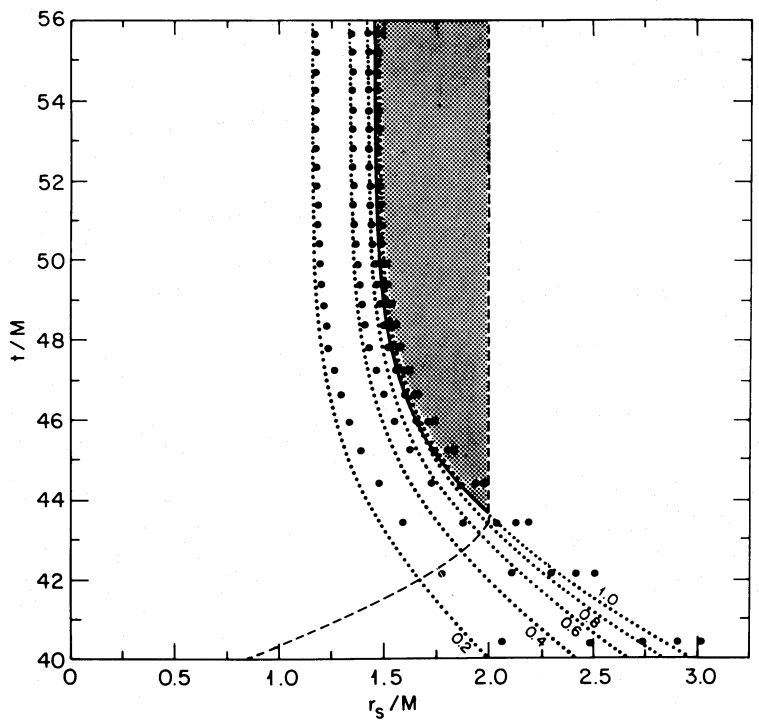

FIG. 9.—Blowup of Fig. 8 at late times. See text for comparison of exact PST results and those obtained here.

© American Astronomical Society • Provided by the NASA Astrophysics Data System

1985ApJ...298...34S

the change in proper time at the center to the change in proper time at infinity (≡ coordinate time at infinity). Its small value shows clearly the degree to which maximal time slicing is successful in holding back the evolution near the center. All the matter is inside the event horizon at this late time, and further integration into the future would not be particularly revealing for this case. Note that the entire evolution proceeds without numerical or physical singularities, a triumph of the choice of gauge and its numerical implementation.

b) *Equilibrium Clusters With Homogeneous Profiles and Circular Orbits*

A second test of our code's ability to evolve collisionless matter in conformity with known, analytic expectations is provided by the case of a homogeneous ball whose particles all move in circular orbits at $t = 0$. The orbits are assumed to be isotropically distributed in the transverse direction perpendicular to the radius vector. This example contrasts with the previous homogeneous dust ball case, in that the configuration here is by construction initially in equilibrium and the orbits are, at least at $t = 0$, nonradial.

Each configuration is again uniquely specified by its nondimensional radius R/M, where R is the Schwarzschild coordinate at the surface and M is the total mass-energy. The mass-energy density profile is again given in the momentarily static Schwarzschild frame by

$$\rho(r_s) = \begin{cases} \dfrac{3M}{4\pi R^3}, & 0 \le r_s \le R, \\ 0, & r_s > R. \end{cases} \tag{70}$$

Now, however, all particles at radius r move with circular velocity

$$v^{\hat{\phi}}(r_s) = V_{\rm cir}(r_s) = \left(\frac{m(r_s)}{r_s}\right)^{1/2} \frac{1}{(1 - 2m(r_s)/r_s)^{1/2}}, \quad (t = 0), \tag{71}$$

where

$$m(r_s) = \tfrac{4}{3}\pi r_s{}^3 \rho(r_s) = M r_s{}^3/R^3 \tag{72}$$

is the mass interior to r_s. Clearly, equilibrium configurations only exist for clusters with $v^{\hat{\phi}}(r_s) < 1$ everywhere which according to equation (71) requires

$$R/M > 3 \text{ (for equilibrium)}. \tag{73}$$

For stability we impose the additional constraint

$$\frac{r_s}{m(r_s)} > 6 \text{ (for stability)} \tag{74}$$

throughout the configuration (Zapolsky 1968). This is the familiar condition in general relativity for the stability of a particle circular orbit in the exterior vacuum around a central mass $m \equiv m(r_s)$. The criterion also applies to a circular orbit in the interior of the collisionless, spherical distribution we have been considering: by Birkhoff's theorem, an orbiting particle at r_s is influenced only by the mass interior to it, $m(r_s)$, which remains constant during a homologous radial perturbation.

Equations (72) and (74) together require that

$$R/M > 6 \text{ (for stability)} \tag{75}$$

for global stability.

We have used our code to evolve equilibrium configurations with homogeneous profiles and circular particle velocities as described above. The results are summarized in Figure 10 for three configurations with $R/M = 6.1$, 5.9, and 3.9 respectively. Plotted are spacetime diagrams for the world lines of fictitious Lagrangian matter tracers in the configurations. For these studies, we chose a somewhat less stringent set of integration accuracy parameters than for the case of homogeneous dust collapse. We used $N_f = 120$ radial grid points (of which 60 covered the matter distribution) and $N_p = 1180$ particles. The time step parameter q was fixed at $q = 0.1$.

In Figure 10*a* the results for $R/M = 6.1$ are shown. In this case, the world lines remain nearly vertical at fixed radii to high accuracy for a total integration time corresponding to almost 16 orbital periods for a particle at the surface. This orbital period T_∞ as measured by an observer as infinity is

$$T_\infty/M = 2\pi(R/M)^{3/2}, \tag{76}$$

which gives $T_\infty/M = 94.7$ for $R/M = 6.1$. This configuration is clearly in stable equilibrium, in accord with equation (75).

In Figure 10*b* the results for $R/M = 5.9$ are shown. Equations (72) and (74) together imply that the outer orbits r_s/M between R/M and $(R/6M)^{1/2}R/M$, i.e., $5.85 \le r_s/M \le 5.9$, are initially unstable. Particles in this unstable region (the inner boundary of which is indicated by an arrow in Fig. 10*b*) undergo inward spiral motion toward the center of the configuration. Upon crossing inside formerly stable orbits within $r_s/M = 5.85$, these particles increase the interior mass of these orbits, driving them unstable in compliance with equation (74). Soon there is an avalanche, and the entire cluster undergoes catastrophic collapse to a black hole. The whole process takes but a dozen orbital periods ($T_\infty/M = 90.0$ for $R/M = 5.9$).

In Fig. 10*c*, the results for $R/M = 3.9$ are plotted. Circular orbits in this configuration satisfying $r_s/m(r_s) < 4$ are not only unstable by equation (74), but they are also *unbound* (energy $E \equiv -p_0 > 1$). The region of unbound, unstable orbits r_s/M thus lies between R/M and $(R/4M)^{1/2}R/M$, i.e., $3.85 \le r_s/M \le 3.9$, in the initial configuration. The inner boundary of this region at $r_s/M = 3.85$ is indicated by the outermost arrow in Fig. 10*c*. The region of bound, unstable orbits lies between $(R/4M)^{1/2}R/M$ and $(R/6M)^{1/2}R/M$, i.e., $3.14 \le r_s/M \le 3.85$; the inner boundary of this region at $r_s/M = 3.14$ is indicated by the innermost arrow in the figure. Orbits within $0 \le r_s/M \le 3.14$ are stable.

Given the above characterization of the circular orbits in the sphere with $R/M = 3.9$ at $t = 0$, it is gratifying to obtain the numerical behavior depicted in Figure 10*c*. In particular, to high accuracy, (1) all particles in the unstable, unbound region (the outer 3.8% of the particles) immediately fly off to infinity; (2) all particles in the unstable, bound region between the arrows move into bound but noncircular orbits, never penetrating within the stable interior region at pericenter; and (3) all particles in the stable interior region, within which $m(r_s)$ stays constant, remain in circular orbits at their initial radii. For this case $T_\infty/M = 48.4$, so the total integration time corresponds to 17 initial periods for a particle at the surface.

The fact that our code accurately distinguishes between stable and unstable as well as bound and unbound orbits provides further indication that it is performing reliably. It is encouraging that it is quite sensitive to numerically small but physically important differences in the initial data. Specifically, a stable sphere with $R/M = 6.1$ evolves quite differently from an unstable sphere with $R/M = 5.9$, etc.

Two features of rather general physical significance emerge

© American Astronomical Society • Provided by the NASA Astrophysics Data System

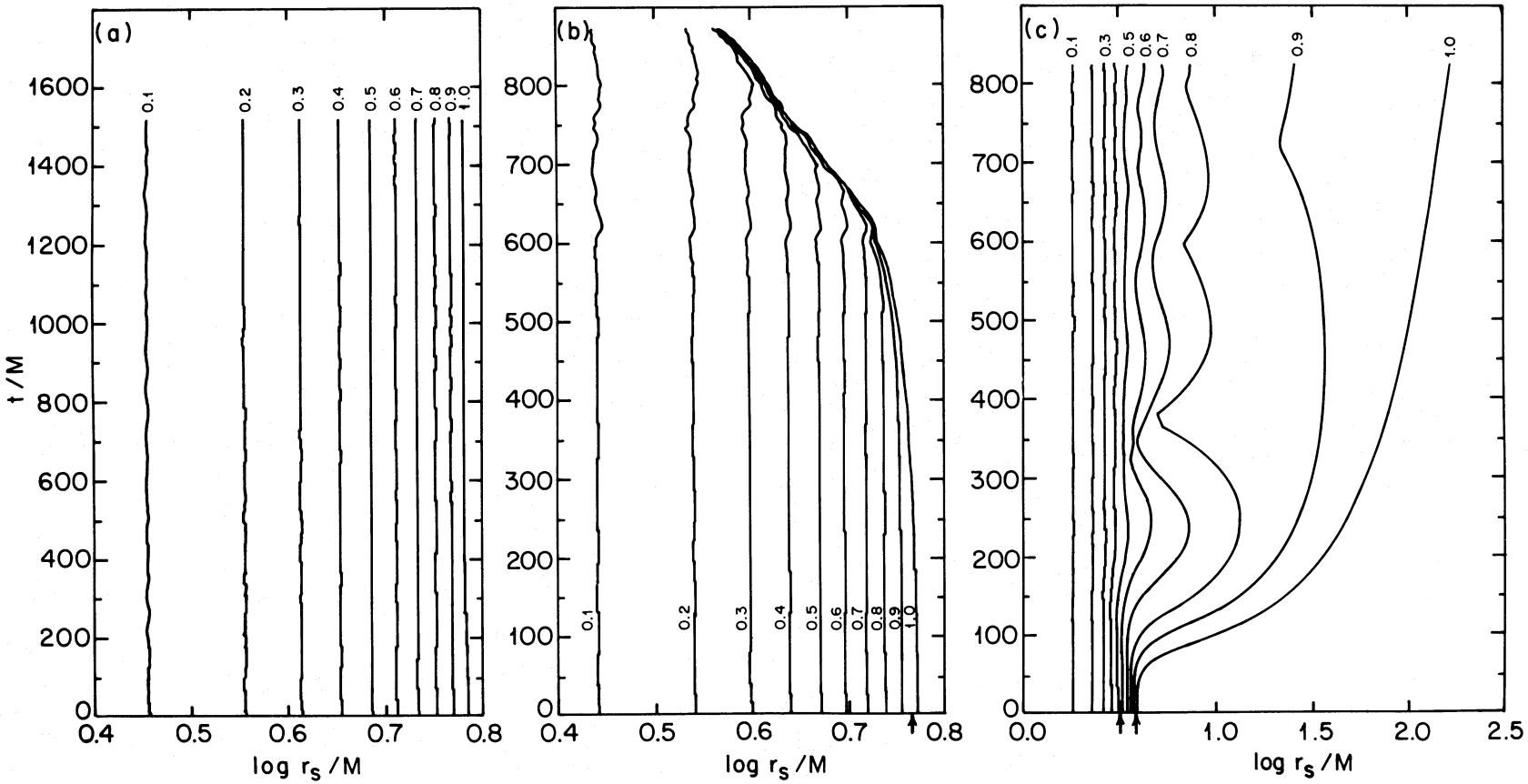

FIG. 10.—Spacetime diagrams for clusters initially in equilibrium with homogeneous profiles and circular orbits. The solid lines are the world lines of Lagrangian matter tracers labeled by the fixed interior rest-mass fraction. Case (*a*) has an initial radius $R/M = 6.1$ and is stable. Case (*b*) has an initial radius $R/M = 5.9$. It is unstable and collapses to a black hole. The collapse is triggered by initially unstable orbits which lie between the arrow and the surface. Case (*c*) has an initial radius $R/M = 3.9$. The orbits between the outer arrow and the surface are unstable and unbound and fly off to infinity. Orbits between the two arrows are unstable but bound. See text.

© American Astronomical Society • Provided by the NASA Astrophysics Data System

1985ApJ...298...34S

from the calculations of homogeneous, circular orbit clusters. First, the instability which triggers collapse results from *collective* behavior. In particular, straightforward analysis of the effective potential governing perturbed circular motion in a homogeneous cluster reveals that circular orbits in a *fixed* background field are stable provided $r_s/m(r_s) > 3$. According to equations (72) and (73), *all* equilibrium clusters satisfy this condition everywhere. This perturbation mode corresponds to a *single* particle whose orbit is perturbed while the other particles remain fixed. Constraint (74), however, corresponds to a collective mode in which all the particles are displaced homologously (i.e., no shell crossing); it is this more stringent, collective mode that governs the stability of the configuration.

Second, we note that the avalanche effect which characterizes the catastrophic collapse of an unstable equilibrium cluster was first predicted by Zel'dovich and Podurets (1965), although they did not appreciate that it could occur in clusters with completely circular orbits. Avalanche-type catastrophic contraction also characterizes the collapse of unstable, equilibrium clusters with isotropic phase space distribution functions, as they anticipated. This fact is demonstrated in Paper II.

This work has been supported by National Science Foundation grants AST 84-15162 and PHY 83-05288.

APPENDIX A

MONOENERGETIC TEST PARTICLE DISTRIBUTION AROUND A SCHWARZSCHILD BLACK HOLE

Consider an isotropic, monoenergetic distribution of identical test particles of mass $m \equiv 1$ around a Schwarzschild black hole of mass M:

$$f(E) = K\delta(E - E_\infty) , \quad K, E_\infty \text{ constant} . \tag{A1}$$

Here $E = -\boldsymbol{p} \cdot \boldsymbol{e}_t = -p_t$ is the conserved "energy at infinity" of a particle. The particle energy measured by a local, stationary, orthonormal observer $\boldsymbol{u} = \boldsymbol{e}_{\hat{t}}$ at Schwarzschild radius r_s is given by

$$E_{\text{local}} \equiv p^{\hat{t}} = -\boldsymbol{p} \cdot \boldsymbol{e}_{\hat{t}} = \frac{E}{(1 - 2M/r_s)^{1/2}} . \tag{A2}$$

The corresponding number density of test particles $n(r_s)$, as measured by $\boldsymbol{u}$, is then

$$n(r_s) = \int f(E) d^3\hat{p} \tag{A3}$$

$$= 4\pi \int f(E)\hat{p}^2 d\hat{p} , \tag{A4}$$

where

$$\hat{p} = [(p^{\hat{t}})^2 - 1]^{1/2} \tag{A5}$$

is the particle 3-momentum. From equations (A2) and (A5) we have

$$\hat{p}^2 d\hat{p} = \frac{\hat{p} E dE}{(1 - 2M/r_s)} = \frac{(E^2 - 1 + 2M/r_s)^{1/2}}{(1 - 2M/r_s)^{3/2}} EdE . \tag{A6}$$

Substituting equations (A1) and (A6) into (A4) yields

$$n(r_s) = 4\pi K \frac{(E_\infty^2 - 1 + 2M/r_s)^{1/2} E_\infty}{(1 - 2M/r_s)^{3/2}} . \tag{A7}$$

For nonrelativistic particles at infinity moving with velocity $v_\infty \ll 1$, we have

$$E_\infty \approx 1 + \tfrac{1}{2} v_\infty{}^2 , \qquad E_\infty{}^2 - 1 \approx 2(E_\infty - 1) \approx v_\infty{}^2 , \tag{A8}$$

so that equation (A7) becomes

$$n(r_s) \approx 4\pi K v_\infty \frac{[1 + 2M/(r_s v_\infty{}^2)]^{1/2}}{(1 - 2M/r_s)^{3/2}} , \tag{A9}$$

or

$$\frac{n(r_s)}{n_\infty} \approx \frac{[1 + 2M/(r_s v_\infty{}^2)]^{1/2}}{(1 - 2M/r_s)^{3/2}} \tag{A10}$$

where

$$n_\infty \equiv 4\pi K v_\infty \tag{A11}$$

© American Astronomical Society • Provided by the NASA Astrophysics Data System

1985ApJ...298...34S

is the number density at infinity in the stationary frame. The corresponding mass-energy density $\rho(r_s)$ measured by $\boldsymbol{u}$ is

$$\rho(r_s) = \int f(E) p^{\hat{t}} d^3\hat{p} \,, \tag{A12}$$

or, using equations (A1), (A2), and (A10)–(A12),

$$\frac{\rho(r_s)}{\rho_\infty} \approx \frac{[1 + 2M/(r_s v_\infty{}^2)]^{1/2}}{(1 - 2M/r_s)^2} \tag{A13}$$

where $\rho_\infty \equiv n_\infty$. Particles everywhere move isotropically with the same locally measured speed $v(r_s)$ given by

$$E_{\text{local}} \equiv \frac{1}{(1 - v^2)^{1/2}} = \frac{E_\infty}{(1 - 2M/r_s)^{1/2}} \,,$$

or

$$v^2(r_s) \approx 2M/r_s \,, \tag{A14}$$

since $E_\infty \approx 1$. Accordingly, the velocity dispersion profiles are given by

$$\langle (v^{\hat{r}})^2 \rangle = \tfrac{1}{2} \langle (v^{\hat{\perp}})^2 \rangle \approx \tfrac{1}{3}(2M/r_s) \,, \tag{A15}$$

where $\hat{\perp}$ denotes the total transverse component in the plane perpendicular to $\boldsymbol{e}_{\hat{r}}$. The mean velocity in any given direction $\mathbf{e}_j$ is

$$\langle v^j \rangle = 0 \,, \tag{A16}$$

by isotropy.

Equations (A10), (A13), (A15), and (A16) constitute the complete density and velocity profiles for the monoenergetic profile equation (A1) (with $v_\infty \ll 1$). To reproduce these profiles conveniently with a particle simulation code, we proceed as follows: distribute particles in coordinate space according to equation (10) and in velocity space according to equation (A14) (isotropically oriented). Confine the particles to a finite region by constructing two rigid, spherical reflecting walls centered on the hole with arbitrary outer radius $r_s = R_2$ and inner radius $r_s = R_1 > 2M$. The particles are then confined to the region $R_1 \leq r_s \leq R_2$. By imposing reflection boundary conditions at the walls, the particles need not be followed out to infinity nor replaced because of capture by the black hole. Moreover, the orbits of only a *finite* number of particles need to be integrated. If the particles have been distributed properly at $t = 0$ and the geodesic equations integrated accurately, the density and velocity profiles, as well as the monoenergetic distribution function, should remain constant for all time $t > 0$.

APPENDIX B

HOMOGENEOUS CLUSTERS WITH INITIALLY TANGENTIAL ORBITS

Consider a spherical configuration of total mass-energy M, Schwarzschild radius R, which at $t = 0$ is everywhere homogeneous:

$$\rho = \frac{3M}{4\pi R^3} \,, \quad 0 \leq r_s \leq R \,. \tag{B1}$$

Suppose further that all the particles in the configuration move initially in tangential orbits, isotropically oriented, with locally measured speed

$$v^{\hat{\phi}}(r_s) = \xi V_{\text{cir}}(r_s) \,, \quad 0 \leq \xi \leq 1 \,, \tag{B2}$$

where ξ is a constant and $V_{\text{cir}}(r_s)$ is the speed of a particle in a circular orbit at Schwarzschild radius r_s about $m(r_s)$, the mass interior to r_s. Accordingly,

$$v^{\hat{\phi}}(r_s) = \xi \left[\frac{m(r_s)}{r_s}\right]^{1/2} \frac{1}{[1 - 2m(r_s)/r_s]^{1/2}} \,, \tag{B3}$$

where

$$m(r_s) = \tfrac{4}{3}\pi\rho r_s{}^3 = M r_s{}^3/R^3 \,. \tag{B4}$$

The subsequent evolution of a *nonequilibrium* configuration with $\xi = 0$ corresponds to closed Friedmann dust collapse to a black hole (or Oppenheimer-Snyder collapse); this case is discussed in § VII*a*. The evolution of an *equilibrium* configuration with $\xi = 1$, when all the particles are in circular orbits, is discussed in § VII*b*. Here we wish to discuss the *intermediate nonequilibrium* case with $0 < \xi < 1$, for which the configuration immediately undergoes collapse. In particular, we wish to determine the critical value of $\xi = \xi_{\text{crit}}$ such that for all $0 < \xi < \xi_{\text{crit}}$, the initial collapse proceeds all the way to a black hole, while for all $\xi_{\text{crit}} < \xi < 1$ the collapse

© American Astronomical Society • Provided by the NASA Astrophysics Data System

1985ApJ...298...34S

is followed by a "bounce" when the surface reaches some smaller radius outside $2M$. In the later case, the "bounce" is followed by a reexpansion of the configuration. Subsequent oscillations of the configuration will, in general, be nonhomologous, due to shell crossing. Such oscillations can then lead to virialization and the establishment of a nonsingular equilibrium state ("relativistic violent relaxation"; see Paper II). This final equilibrium configuration will no longer be homogeneous nor consist of purely tangential orbits.

The quantity $\xi_{\rm crit}$ depends on M/R, the initial compaction of the configuration. Here we will restrict our analysis to *initially* Newtonian configurations satisfying

$$M/R \ll 1 . \tag{B5}$$

Generalization to large initial M/R is straightforward.

Examine the orbits of the particles in the spherical configuration. By equations (B3)–(5), the particles are all nonrelativistic, with energies per unit mass $\tilde{E} \equiv -p_t/m$ satisfying $\tilde{E} - 1 \ll 1$. At $t = 0$ all the particles are at apocenter, since their velocities are transverse and $\xi < 1$; hence, they all immediately plunge radially inward. What is the necessary condition that permits a black hole to form during this initial implosion? The maximum angular momentum per unit mass for the capture of a nonrelativistic particle onto a central hole of mass m is

$$\tilde{l}_{\rm max}(m) = 4m \tag{B6}$$

(see, e.g., Shapiro and Teukolsky 1983, exercise [12.9]). Consider then a particle, initially at r_s, which, before it reaches pericenter and flies back out, plunges inside the black hole formed by the collapse of the mass interior to it. Such a particle must have an initial tangential velocity satisfying

$$v^{\phi} r_s < \tilde{l}_{\rm max}[m(r_s)] = 4m(r_s) \qquad \text{(for capture)} . \tag{B7}$$

In writing equation (B7) we assume that in falling radially inward the particle moves without shell crossing (which is the case when the configuration collapses to a black hole). We invoke Birkhoff's theorem in using equation (B6) with $m = m(r_s)$.

When $M/R \ll 1$, equations (B3) and (B4) imply

$$v^{\phi}(r_s) \approx \xi \left[\frac{m(r_s)}{r_s}\right]^{1/2} . \tag{B8}$$

Substituting equation (B8) into (B7) yields the constraint

$$\frac{M}{R} \geq \frac{m(r_s)}{r_s} \gtrsim \frac{\xi^2}{16} \qquad \text{(for capture)} , \tag{B9}$$

where the first inequality follows from equation (B4). According to equation (B9), capture does not occur unless particles initially at the *surface* of the configuration at $r_s = R$ are in capture orbits. That is, if particles at the surface are not in capture orbits, neither are particles anywhere else, and no black hole forms. Thus the critical condition for the collapse of the configuration to a black hole is

$$\xi < \xi_{\rm crit} \approx 4(M/R)^{1/2} \qquad \text{(for black hole)} , \tag{B10}$$

which becomes exact as M/R goes to zero.

APPENDIX C

HOMOGENEOUS NEWTONIAN CLUSTERS WITH INITIALLY TANGENTIAL ORBITS

Consider the dynamical evolution of a homogeneous, Newtonian sphere of mass M, radius R_0 whose particles everywhere move on randomly oriented tangential orbits with speed

$$v^{\phi} = \xi V_{\rm cir}(r) , \qquad \xi = \text{constant} \tag{C1}$$

at $t = 0$. Here $V_{\rm cir}(r)$ is the local circular velocity given by

$$V_{\rm cir}(r) = (m(r)/r)^{1/2} , \tag{C2}$$

where $m(r)$ is the mass interior to r. Such a sphere will subsequently undergo periodic, homologous oscillations. It will remain homogeneous at all times, expanding beyond R_0 and returning one-half period later if $1 < \xi < 2^{1/2}$, while contracting inside R_0 and subsequently returning if $0 < \xi < 1$. If $\xi = 0$, the configuration undergoes homogeneous collapse to a singularity, while if $\xi = 1$, it remains in stable equilibrium; if $\xi \geq 2^{1/2}$ it is unbound and expands out to infinity.

The key features of the motion of such a sphere can be simply derived. Focus on a fiducial particle in the sphere, e.g., the particle at radius $r = r_0$ at $t = 0$. It moves according to the dynamical equation

$$\ddot{r} = -\frac{m(r)}{r^2} + \frac{j^2}{r^3} , \tag{C3}$$

© American Astronomical Society • Provided by the NASA Astrophysics Data System

1985ApJ...298...34S

subject to the initial conditions

$$r = r_0 \quad \text{and} \quad \dot{r} = 0 \quad \text{at} \quad t = 0 . \tag{C4}$$

In equation (C3), j is the conserved angular momentum per unit mass. Assuming no shell crossing (justified self-consistently below), we have

$$m(r) = Mr_0^3/R_0^3 = \text{constant in time} \tag{C5}$$

and

$$j = (v^{\hat{\phi}}r)_{t=0} = \xi(Mr_0^4/R_0^3)^{1/2} = \text{constant in time} . \tag{C6}$$

Defining a nondimensional particle radius

$$x \equiv r/r_0 \tag{C7}$$

and substituting equations (C5)–(C7) into (C3) and (C4) yields

$$\ddot{x} = -\frac{M}{R_0^3 x^2} + \frac{\xi^2 M}{R_0^3 x^3} , \tag{C8}$$

and

$$x = 1 \quad \text{and} \quad \dot{x} = 0 \quad \text{at} \quad t = 0 . \tag{C9}$$

Since equations (C8) and (C9) do not depend on r_0, the motion is indeed homologous as claimed (and hence there can be no shell crossing). Equations (C8) and (C9) are effectively equivalent to the equations of motion of a particle of radius x with specific angular momentum $j_{\text{eff}} \equiv \xi(M/R_0^3)^{1/2}$ around a fixed central mass $M_{\text{eff}} \equiv M/R_0^3$. The first integral of equation (8) yields the conserved energy for this particle:

$$E = \frac{1}{2}\dot{x}^2 - \frac{M_{\text{eff}}}{x} + \frac{j_{\text{eff}}^2}{2x^2} = \text{constant} , \tag{C10}$$

which can be evaluated at $t = 0$, using equation (9),

$$E = -M_{\text{eff}} + \frac{j_{\text{eff}}^2}{2} . \tag{C11}$$

Setting $\dot{x} = 0$ in equation (C10) and solving for the turning points yields

$$x_1 = 1$$

$$x_2 = \xi^2/(2 - \xi^2) .$$

Thus the configuration expands beyond R_0 if $\xi > 1$ and contracts if $\xi < 1$, as claimed. For $0 < \xi < 2^{1/2}$ the motion is periodic with period

$$P = \pi M_{\text{eff}}/(2|E|^3)^{1/2}$$

$$= 2\pi\left[\frac{R_0^3}{M(2 - \xi^2)}\right]^{1/2} . \tag{C13}$$

Since the density is homogeneous, the mean (i.e., radial) velocity throughout the sphere is linearly proportional to radius r at each instant of time. Straightforward solution of the familiar orbit equations (C8) and (C9) yields $x(t)$, from which the matter density $\rho(t)$ and mean velocity $\langle v^{\hat{r}}(t, r)\rangle$ throughout the oscillating sphere can be readily obtained:

$$\rho(t) = \frac{3M}{4\pi R_0^3}\frac{1}{x^3(t)} , \tag{C14}$$

$$\langle v^{\hat{r}}(t, r)\rangle = \dot{r} = \pm r\left\{\frac{4\pi\rho(t)}{3}\left[2 + (\xi^2 - 2)x(t) - \frac{\xi^2}{x(t)}\right]\right\}^{1/2} . \tag{C15}$$

APPENDIX D

EQUILBRIUM CLUSTERS WITH PARABOLIC PROFILES AND CIRCULAR ORBITS

The stability and dynamical evolution of equilibrium clusters with *homogeneous* profiles and circular orbits was discussed in § VIII*b*. Here we address the same issues for clusters with *parabolic* mass-energy density profiles:

$$\rho(r_s) = \begin{cases} \rho_c(1 - r_s/R^2) , & 0 \le r_s \le R , \\ 0 , & r_s > R , \end{cases} \tag{D1}$$

© American Astronomical Society • Provided by the NASA Astrophysics Data System

1985ApJ...298...34S

where r_s is the Schwarzschild radial coordinates. Substituting equation (D1) into the mass-energy integral equation (63) yields

$$\rho_c = \frac{15}{8\pi}\frac{M}{R^3} \tag{D2}$$

for the central density and

$$\frac{m(r_s)}{M} = \left(\frac{r_s}{R}\right)^3\left[\frac{5}{2} - \frac{3}{2}\left(\frac{r_s}{R}\right)^2\right] \tag{D3}$$

for the total mass-energy fraction interior to r_s. For an equilibrium configuration in which the particles everywhere move on circular orbits isotropically oriented perpendicular to $\boldsymbol{e}_r$, the particle speed is

$$v^{\hat{\phi}}(r_s) = V_{\rm cir}(r_s) = \left[\frac{m(r_s)}{r_s}\right]^{1/2}\frac{1}{[1 - 2m(r_s)/r_s]^{1/2}}\,. \tag{D4}$$

Equilbrium models are possible only for velocities $v^{\hat{\phi}}(r_s)$ satisfying

$$v^{\hat{\phi}}(r_s) < 1 \qquad \text{(for equilbrium)}\,, \tag{D5}$$

which, substituting equation (D4) into (D5), implies

$$m(r_s)/r_s < \tfrac{1}{3} \qquad \text{(for equilbrium)}\,. \tag{D6}$$

According to equation (D3), the maximum value of $m(r_s)/r_s$ on $r_s/R \in [0, 1]$ occurs at $r_s/R = (\frac{5}{6})^{1/2}$. Imposing constraint (D6) at this point yields an equilibrium condition on R, the radius of a parabolic configuration:

$$R/M > \tfrac{25}{8} = 3.125 \qquad \text{(for equilibrium)}\,. \tag{D7}$$

In order that the circular orbits be stable, it is both necessary and sufficient that the inequality

$$m(r_s)/r_s < \tfrac{1}{6} \qquad \text{(for stability)} \tag{D8}$$

hold in addition. Imposing constraint (D8) at $r_s/R = (\frac{5}{6})^{1/2}$ yields a more stringent condition on R:

$$R/M > \tfrac{25}{4} = 6.25 \qquad \text{(for stability)}\,. \tag{D9}$$

REFERENCES

Antonov, V. A. 1962, *Vestn. Leningr. Gos. Univ.*, No. 19, p. 96.
Arnowitt, R., Deser, S., and Misner, C. W. 1962, in *Gravitation*, ed. L. Witten (New York: Wiley), p. 227 (ADM).
Bardeen, J. M., and Piran, T. 1983, *Phys. Repts*, **96**, 205.
Begelman, M. C., Blandford, R. D., and Rees, M. J. 1984, *Rev. Mod. Phys.*, **56**, 255.
Deruelle, N., and Piran, T. 1983, ed., *Gravitational Radiation, Les Houches 1982* (Amsterdam: North Holland).
Eardley, D. M., and Smarr, L. 1979, *Phys. Rev. D.*, **19**, 2239.
Einstein, A. 1939, *Ann. Math.*, **40**, 922.
Fackerell, E. D. 1968, *Ap. J.*, **153**, 643.
———. 1970, *Ap. J.*, **160**, 859.
Fackerell, E. D., Ipser, J. R., and Thorne, K. S. 1969, *Comments Ap. Space Phys.*, **1**, 134.
Hawking, S. W., and Ellis, G. F. R. 1973, *The Large Scale Structure of Space-Time* (Cambridge: Cambridge University Press).
Henon, M. 1973, *Astr. Ap.*, **24**, 229.
Ipser, J. R. 1969*a*, *Ap. J.*, **156**, 509.
———. 1969*b*, *Ap. J.*, **158**, 17.
———. 1980, *Ap. J.*, **238**, 1101.
Ipser, J. R., and Thorne, K. S. 1968, *Ap. J.*, **154**, 251.
Katz, J., and Horwitz, G. 1974, *Ap. J.*, **194**, 439.
Lightman, A. P., Press, W. H., Price, R. H., and Teukolsky, S. A. 1975, *Problem Book in Relativity and Gravitation* (Princeton: Princeton University Press).
Lightman, A. P., and Shapiro, S. L. 1978, *Rev. Mod. Phys.*, **50**, 437.
Lynden-Bell, D., and Sanitt, N. 1969, *M.N.R.A.S.*, **143**, 167.
Misner, C. W., Thorne, K. S., and Wheeler, J. A. 1973, *Gravitation* (San Francisco: Freeman).
Morse, P. M., and Feshbach, H. 1953, *Methods of Theoretical Physics*, Vol. **1** (New York: McGraw-Hill).
Oppenheimer, J. R., and Snyder, H. 1939, *Phys. Rev.* **56**, 455.
Petrich, L., Shapiro, S. L., and Teukolsky, S. A. 1985, *Phys. Rev. D*, **31**, 2459 (PST).
Shapiro, S. L., and Teukolsky, S. A. 1979, *Ap. J.* (*Letters*), **234**, L177.
———. 1980, *Ap. J.*, **235**, 199.
———. 1983, *Black Holes, White Dwarfs and Neutron Stars: The Physics of Compact Objects* (New York: Wiley).
———. 1985*a*, *Ap. J.*, **298**, 58 (Paper II).
———. 1985*b*, *Ap. J.* (*Letters*), **292**, L41 (Paper III).
Smarr, L. 1979, ed. *Sources of Gravitational Radiation* (Cambridge: Cambridge University Press).
Smarr, L., and York, J. W. 1978*a*, *Phys. Rev. D*, **17**, 1945.
———. 1978*b*, *Phys. Rev. D*, **17**, 2529.
Spitzer, L. 1975, in *IAU Symposium 69, Dynamics of Stellar Systems*, ed. A. Hayli (Dordrecht: Reidel), p. 3.
———. 1985, in *IAU Symposium 113, Dynamics of Star Clusters*, ed. J. Goodman and P. Hut (Dordrecht: Reidel), p. 109.
Stark, R., and Piran, T. 1985, in preparation.
Suffern, K. G., and Fackerell, E. D. 1976, *Ap. J.*, **203**, 477.
Synge, J. L. 1934, *Trans. Roy. Soc. Canada, III*, **28**, 127.
Walker, A. G. 1936, *Proc. Edingurgh Math. Soc.*, **4**, 238.
York, J. W. 1979, in *Sources of Gravitational Radiation*, ed. L. Smarr (Cambridge: Cambridge University Press).
Zapolsky, H. S. 1968, *Ap. J.* (*Letters*), **153**, L163.
Zel'dovich, Ya. B., and Novikov, I. D. 1971, *Relativistic Astrophysics*, Vol. **1** (Chicago: University of Chicago Press).
Zel'dovich, Ya. B., and Podurets, M. A. 1965, *Astr. Zh.*, **42**, 963 (English transl. in *Soviet Astr.—AJ*, **9**, 742 [1966]).

STUART L. SHAPIRO and SAUL A. TEUKOLSKY: Space Sciences Bldg., Cornell University, Ithaca, NY 14853

© American Astronomical Society • Provided by the NASA Astrophysics Data System